

Evidence for grid cells in a human memory network

Christian F. Doeller^{1,2}, Caswell Barry^{1,3,4} & Neil Burgess^{1,2}

Grid cells in the entorhinal cortex of freely moving rats provide a strikingly periodic representation of self-location¹ which is indicative of very specific computational mechanisms^{2–4}. However, the existence of grid cells in humans and their distribution throughout the brain are unknown. Here we show that the preferred firing directions of directionally modulated grid cells in rat entorhinal cortex are aligned with the grids, and that the spatial organization of grid-cell firing is more strongly apparent at faster than slower running speeds. Because the grids are also aligned with each other^{1,5}, we predicted a macroscopic signal visible to functional magnetic resonance imaging (fMRI) in humans. We then looked for this signal as participants explored a virtual reality environment, mimicking the rats' foraging task: fMRI activation and adaptation showing a speed-modulated six-fold rotational symmetry in running direction. The signal was found in a network of entorhinal/subicular, posterior and medial parietal, lateral temporal and medial prefrontal areas. The effect was strongest in right entorhinal cortex, and the coherence of the directional signal across entorhinal cortex correlated with spatial memory performance. Our study illustrates the potential power of combining single-unit electrophysiology with fMRI in systems neuroscience. Our results provide evidence for grid-cell-like representations in humans, and implicate a specific type of neural representation in a network of regions which supports spatial cognition and also autobiographical memory.

Grid cells recorded in medial entorhinal cortex of freely moving rodents fire whenever the animal traverses the vertices of an equilateral triangular grid covering the environment (see Fig. 1a), and may provide a neural substrate for path integration^{1–3,6}. However, it is not known whether or not grid cells exist in humans, or how widespread the network of neurons with grid-like firing is, although the pre- and parasubiculum⁷ and posterior parietal cortex⁸ have been implicated.

Could grid-cell firing be detected in the functional magnetic resonance imaging (fMRI) signal, which reflects changes in metabolic activity across thousands of individual neurons? The grid patterns of neighbouring cells are offset so as to 'tile' the environment¹, making systematic variation in population activity with position unlikely. However, three factors may allow detection using fMRI. The first factor is that the angular orientation of the grids relative to the environment appears to be constant across cells, whether they are neighbouring¹ or farther apart⁵ (Supplementary Fig. 1), and rotate coherently when salient distal cues are rotated^{1,6}. The other two factors result from new analyses presented here. The second factor being that firing of 'conjunctive' grid cells, found in the deeper layers of entorhinal cortex⁶ and in pre- and parasubiculum⁷, is modulated by running direction⁶. Here we show that the directions of modulation of conjunctive grid cells are aligned with the main axes of the grids (Fig. 1a–c). These first two factors will create systematic differences in neural population dynamics for runs aligned or misaligned with the main axes of the grids (Fig. 2). A third factor is running speed: the rate⁶ and inter-burst frequency¹⁰ of grid-cell firing, and the frequency with

which individual firing fields in a grid are sampled, increase with running speed. In addition, we show that the spatial organization of grid-cell firing is more strongly apparent during fast running than during slow running and immobility (Fig. 1d; see Methods for details and Supplementary Figs 2–6 for further analyses and recording locations). Thus, entorhinal grid cells form a coherent population in which the common effects of orientation and speed of movement could produce a macroscopic signal visible with fMRI.

We recorded whole-brain fMRI data while human participants navigated within a virtual reality arena, mimicking the foraging task

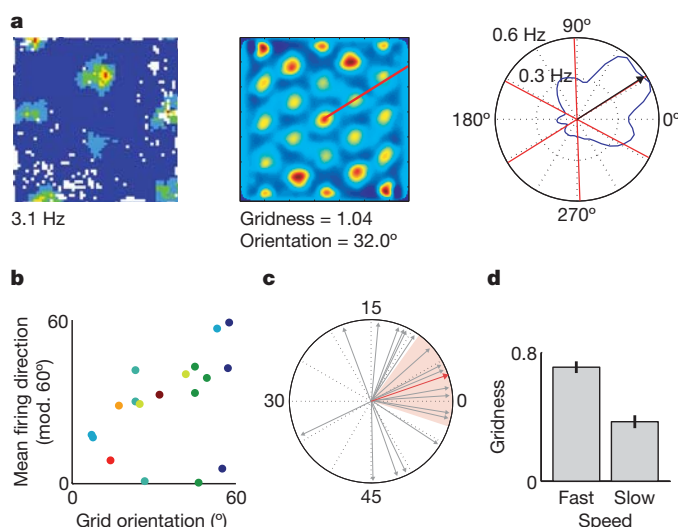


Figure 1 | The mean firing directions of directional grid cells are aligned with the grid. **a**, The left panel shows the firing rate map of a typical 'conjunctive' directional grid cell showing firing rate as a function of the rat's location within a 1 m² box (red, high firing rate; blue, low rate; white, unvisited location; peak rate 3.1 Hz). The middle panel shows the spatial autocorrelogram constructed from the rate map. The right panel shows the polar firing rate map for the same cell. The black arrow indicates mean firing direction. Red lines indicate the main axes of the grid firing pattern identified from the spatial autocorrelogram (see middle). **b**, Scatter plot of all directional grid cells ($n = 18$) showing grid orientation versus circular mean firing direction, modulo 60°. Cells from different rats ($n = 8$) are coloured differently. **c**, Angular difference between the circular mean firing direction of each cell and the nearest axis of its grid-like firing pattern is not distributed uniformly (Rayleigh test of uniformity; $P = 0.007$) and is significantly clustered around zero (Monte Carlo simulation; $P < 0.001$). The red arrow shows the mean difference (3.15°); red shaded area indicates the 95% confidence interval. **d**, The spatial organization of grid cell firing is less strongly apparent during slow movement and immobility than during fast movement. The bar graph shows mean gridness (a measure of six-fold spatial periodicity, see Methods) score for 113 grid cells, separately for fast and slow movements (median split); paired t -test, $P = 2.2 \times 10^{-11}$. Error bars show s.e.m. over cells.

¹UCL Institute of Cognitive Neuroscience, London WC1N 3AR, UK. ²UCL Institute of Neurology, London WC1N 3BG, UK. ³UCL Department of Cell and Developmental Biology, London WC1E 6BT, UK. ⁴UCL Institute of Behavioural Neuroscience, University College London, London WC1H 0AP, UK.

in rodents (see Methods for details). The arena comprised a grassy plain bounded by a cylindrical cliff, containing a single intra-maze landmark and surrounded by a background scene providing orientation cues rendered at infinity (Fig. 2a). Participants collected and replaced objects found within the arena. Memory was measured as the proximity of the replacement location to the correct location (Supplementary Fig. 7 and ref. 11).

If orientationally aligned grid-cell firing is present, there should be an effect of running direction with six-fold rotational symmetry, reflecting the differences between running aligned or misaligned to the grid axes, and this effect should be modulated by running speed (Fig. 2b–d). We defined an anatomical region of interest (ROI) on the entorhinal cortices, and examined one-half of the fMRI data for modulation by running direction and speed to find the orientation of potential grids within each participant's entorhinal cortex. Briefly, we used a quadrature filter to identify the orientation of any six-peaked sinusoidal modulation of signal as a function of running direction and speed: providing the potential grid orientation in each voxel (Supplementary Fig. 8 and Methods). The potential grid orientations during fast runs were significantly clustered across voxels in the ROI in 34 out of 42 participants (Rayleigh test, accounting for spatial smoothing, on each participant; $P \ll 0.00001$ for the population, Monte Carlo simulation; Supplementary Fig. 9). The mean grid orientation for the entorhinal ROI (φ) was defined as the population vector (vector sum of orientations weighted by amplitude), and calculated for data corresponding to fast, medium and slow runs.

We then examined the second half of the data for differential activation for fast, medium and slow runs aligned versus misaligned to each participant's mean grid orientation. We looked for sinusoidal modulation of activation with six-fold rotational symmetry aligned with each participant's mean grid orientation across the whole brain

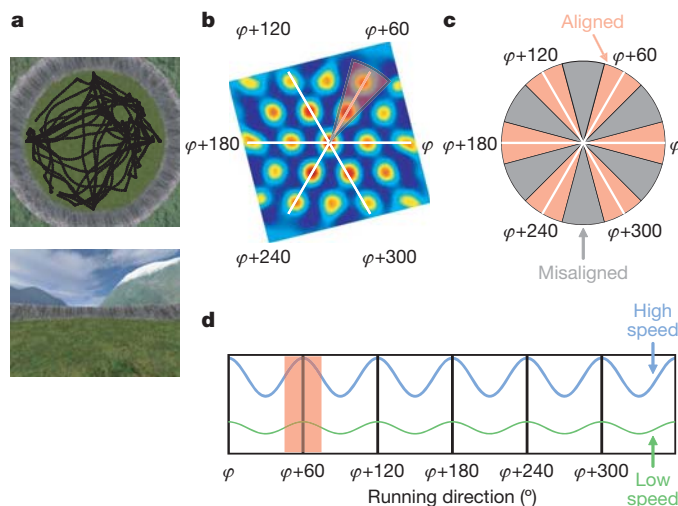


Figure 2 | fMRI: virtual reality arena and experimental logic. **a**, Human participants ($n = 42$) explored a circular virtual reality environment, bounded by a cliff and surrounded by orientation cues (mountains), finding objects and having to replace them in the correct locations. Top panel: aerial view, including one participant's virtual trajectory (black line). Bottom panel: participant's view. **b**, Spatial autocorrelogram of a typical grid cell showing the three main axes of the grid (white lines) and a 30° sector aligned with the grid (red). φ indicates mean grid orientation to which the grid shown is aligned. **c**, Schematic of running directions aligned (red) and misaligned (grey) with the grid. **d**, Given the alignment of directionally modulated grid cells with the grid and the constant grid orientation across cells (Fig. 1b), we predicted a sinusoidal modulation of fMRI signal by running direction with six-fold rotational symmetry, and a stronger effect for faster (blue) than slower (green) runs (see Fig. 1d). Note that the absolute orientation of the pattern (mean grid orientation, φ) will not be known a priori.

(using the regressor $\cos(6[\theta(t) - \varphi])$ where $\theta(t)$ is running direction; Supplementary Fig. 8). We found a significant activation in the right entorhinal cortex for fast runs (Fig. 3a, b). Direct comparison of activation for fast runs aligned versus misaligned to each participant's mean grid orientation showed a similar effect (Fig. 3d). Similar sinusoidal modulations were present in left entorhinal cortex, although slightly less reliably than on the right, and in the mean response of the entorhinal ROI (Supplementary Fig. 10). No activation elsewhere in the brain reached the significance level for this whole-brain analysis. Equivalent analyses for medium or slow runs, or looking for four- or eight-fold (Fig. 3b, c), or even five- or seven-fold, rotational symmetry (Supplementary Fig. 11) failed to show significant activation. No significant activation was found when the analyses applied to the entorhinal ROI were performed to control ROIs in the posterior right hippocampal location associated with memory performance in this task¹¹ or the visual cortical location showing adaptation to running direction (below) (see Supplementary Fig. 12). Supplementary Figs 13–15 show control analyses of behaviour in rats and humans.

Consistent with grid cells, the mean grid orientations in the six-fold symmetry model varied randomly between participants, ruling out a role for specific visual features of the environment (Supplementary Fig. 16). Notably, the coherence of the potential grid orientations in each participant's right entorhinal cortex was significantly correlated with that participant's spatial memory performance (Fig. 3f). This parallels findings that entorhinal cortex activation can predict memory performance^{12,13}, and provides a first indication that grid-like representations might usefully guide behaviour in mammals.

An independent indicator of variation in the dynamics of neuronal activity is provided by fMRI adaptation^{14–17}, that is, reduced signal from activation of a representation that was recently active compared to a previously inactive one. During runs aligned with the grid, a smaller proportion of grid cells will fire but will do so at a higher rate, whereas more grid cells will be active during misaligned runs but at a lower rate (Supplementary Fig. 17). Given the complex nonlinear dynamical relationship between neuronal activation and fMRI adaptation⁹ we predicted that differences in the dynamics of neuronal activity when running aligned to the grids compared to misaligned would cause differences in fMRI adaptation, and that these differences would also vary with running speed.

We first checked whether the more basic effect of fMRI adaptation to running direction occurred within our virtual navigation paradigm. We made separate adaptation regressors (the logarithm of the time since last running in the current direction) for fast, medium and slow runs. We found significant adaptation to running direction in visual cortex extending into posterior parahippocampal/lingual and retrosplenial cortices, with larger effects for fast than for slow runs (see Fig. 4a, b). The adaptation effect is independent of variations in angular velocity (see Methods) and is consistent with adaptation to the background visual scene (which is rendered at infinity; viewing direction is the same as running direction), as previously found with static scenes in similar areas^{14,16}. It is also consistent with view-specific single-unit responses in humans¹⁸ or with the presence of head-direction cells¹⁹, which have been reported in retrosplenial cortex²⁰.

Given the robust fMRI adaptation to virtual running direction, we tested our specific prediction that adaptation in entorhinal cortex is modulated by running direction with 60° periodicity and by running speed. Accordingly we looked for regions showing a reduction in fMRI signal according to how recently participants were running at 60° to the current direction, which was greater for fast than for slow running. Unlike our analysis of whole-brain activation as a function of mean grid orientation in the entorhinal ROI (Fig. 3), this analysis can be directly applied to the whole brain without reference to specific ROIs. As predicted, right entorhinal cortex (extending into subiculum) showed 60° shifted directional adaptation, independent of any effect of basic directional adaptation, as did regions in posterior parietal, lateral temporal and medial prefrontal cortices (see Fig. 4c). Medial

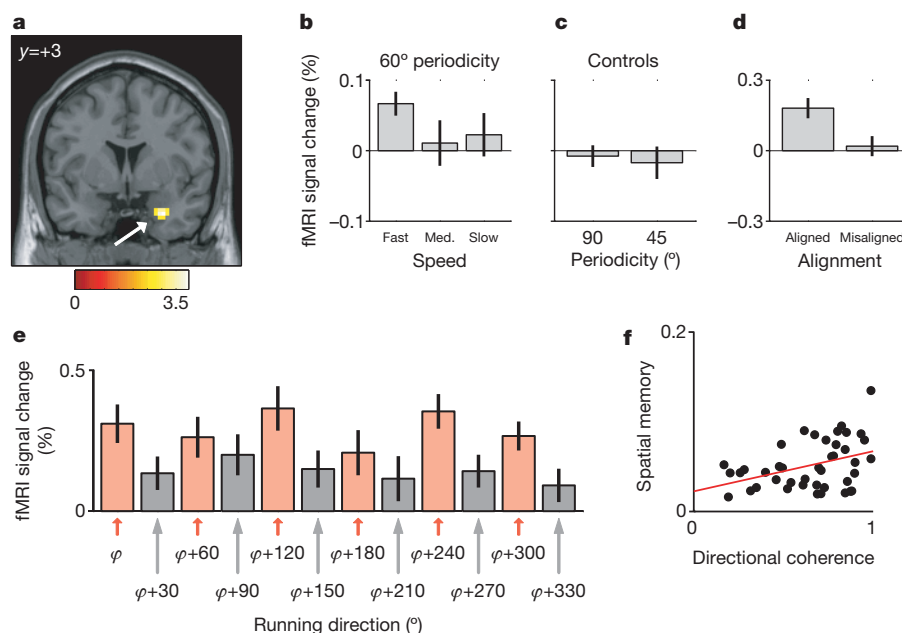


Figure 3 | Modulation of entorhinal cortical activity by running direction with six-fold rotational symmetry, and correlation with spatial memory. **a**, Sinusoidal modulation of activity by running direction with six-fold rotational symmetry. The orientation of potential grids in each participant's entorhinal cortex was estimated on one-half of the data, and the correspondingly aligned sinusoidal regressor was fitted to the other half of the data, showing a significant modulation only in right entorhinal cortex. Plot shows fMRI activation for fast runs on an aligned structural template; colour bar indicates *t*-statistic; all reported effects of whole-brain analyses are significant at $P < 0.001$ uncorrected; the *t*-image is thresholded at $P < 0.01$ for display purposes; peak Montreal Neurological Institute (MNI) coordinates: 30/3/-30; peak *z*-score = 3.59. **b**, Directional modulation depends on running speed, being present for fast runs, but not for medium (Med.) or slow runs. **c**, Directional modulation during fast runs has 60° directional periodicity, not 90° or 45° (that is, six-fold rather than four- or

parietal cortex also showed 60° shifted directional adaptation, in addition to the basic directional adaptation described above, consistent with the presence of both visual/head-direction and grid-like representations (see Supplementary Fig. 18). The adaptation effect in all of these regions was strongly modulated by the participants' virtual running speed, being higher for fast compared to slow runs (Fig. 4d); the effect was specific to 60° rather than 45° or 90° shifted directional adaptation (Fig. 4e).

Do these remote regions showing 60° shifted directional adaptation also show the sinusoidal modulation of activation seen in entorhinal cortex during fast running, consistent with the presence of grid-like representations in these regions too? We examined the mean response to the sinusoidal regressor defined in entorhinal cortex in 8-mm-radius ROIs centred on the locations of peak adaptation. The responses in medial prefrontal (one-tailed *t*-test; $P = 0.008$), medial parietal ($P = 0.002$) and lateral temporal (left, $P = 0.019$; right, $P = 0.0005$) ROIs, but not the posterior parietal ROI ($P = 0.058$), reached significance for this specific prediction. Overall, these results suggest a network of regions containing coherently aligned neural representations with six-fold rotational symmetry, although the responses in remote regions were weaker than in right entorhinal cortex (for example, not reaching significance in the initial whole-brain split-half analysis), possibly reflecting a lower concentration of grid-like cells.

Our results provide the first evidence that human entorhinal cortex encodes virtual movement direction with six-fold symmetry, consistent with a coherently-oriented population of grid cells similar to those found in rat entorhinal cortex^{1,5,6} and pre- and parasubiculum⁷. The dependence of directional modulation on running speed is consistent with the effects of speed on the firing rate^{6,10} and apparent

eight-fold rotational symmetry). Bar plots in **b** and **c** show the mean amplitude of sinusoidal modulation for the peak voxel in **a**. **d**, Activation for aligned (within 15° of the main axes of the grid, see Fig. 2c) and misaligned fast runs relative to baseline (epochs of no movement in the environment) in the peak voxel shown in **a**, confirming the sinusoidal modulation effect. **e**, To examine the pattern underlying these effects, we plotted the average fMRI signal over the entire time series of all voxels in the entorhinal ROI for all directions of aligned (red) and misaligned (grey) fast runs, relative to baseline (see Fig. 2c). **f**, The coherence of the potential grid orientations in each participant's right entorhinal cortex (mean length of resultant direction vector) correlated significantly with that participant's spatial memory (1/mean distance of object replacement locations from correct locations; range = 7.4–61.7 virtual metres; mean = 25.4, Spearman's $\rho = 0.32$, $P = 0.039$). Each dot represents one participant. All bars show mean and s.e.m. over participants.

spatial organization (Fig. 1d) of grid cells, whereas effects of speed on other aspects of behaviour may also contribute (see for example, Supplementary Fig. 14). The relationship to spatial memory of the directional coherence of potential grids across entorhinal cortex provides a first indication that grid-like representations might usefully guide behaviour.

Because we can only measure effects of direction and speed (not location) in the fMRI signal, our findings could reflect the presence of grid cells, or movement-related responses from head direction¹⁹, or 'conjunctive' directional grid^{6,7} cells, if they form coherent populations whose firing has six-fold rotational symmetry. We showed that conjunctive grid cells from rat entorhinal cortex have such an organization (Fig. 1). Our finding of similar and aligned fMRI responses from subicular, posterior/medial parietal, lateral temporal, and medial prefrontal cortices indicate that populations with similar properties also exist elsewhere, a prediction directly testable in rodents (see also refs 7, 8). These results outline a circuit for navigation, consistent with suggestions that medial and lateral temporal, posterior and medial parietal and medial prefrontal areas cooperate to support spatial cognition^{2,8,11,21,22}, and implicate a specific type of underlying neural representation.

Our study illustrates the ability to infer neural representations in humans by using fMRI in conjunction with single-unit recording in behaving animals, promising a coherent understanding of behaviour at the neural and systems levels. The observed grid-like representations support spatial memory (Fig. 3f) and are found in a circuit of regions which markedly overlaps the network for autobiographical memory and imagery (for example, refs 21, 23, 24). These types of regularly repeating representation may provide a clue to the neural basis of autobiographical memory, perhaps encoding temporal as

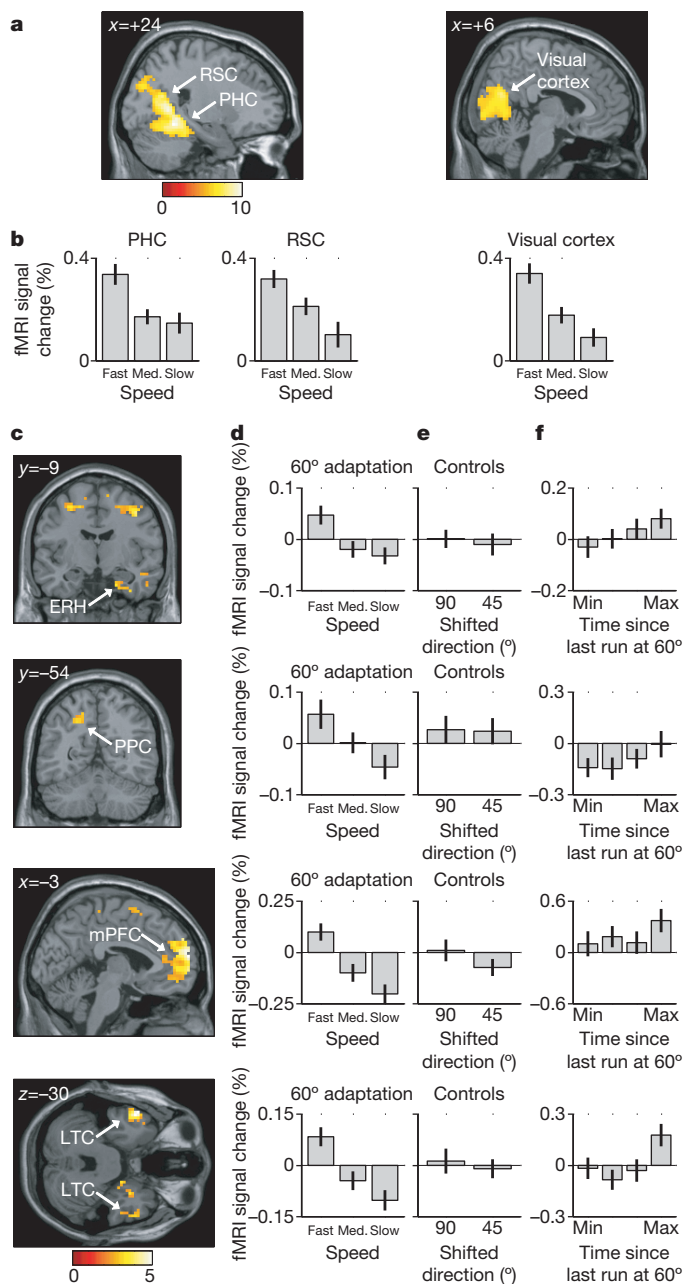


Figure 4 | fMRI adaptation to running direction and to runs at 60° from it. **a**, Activity in parahippocampal (PHC; 24/−48/12; $z = 7.13$), retrosplenial (RSC; 18/−57/18; $z = 7.16$) and visual (peak at 18/−69/15; $z = 7.11$) cortices shows adaptation to absolute running direction (regressor: $\log[\text{time since last run in current direction}]$). **b**, Adaptation is greater for faster runs, showing the adaptation effect for the peak voxels in the three regions for fast, medium (Med.) and slow runs. **c**, A speed-dependent fMRI adaptation to runs at 60° from the current direction (regressor: $\log[\text{time since last run at 60° from the current direction}]$) is seen in a network of regions, including entorhinal cortex extending into subiculum (ERH; 21/−9/−30; $z = 3.28$), anterior entorhinal/perirhinal (33/0/−27; $z = 3.69$), posterior parietal (PPC; −18/−54/45; $z = 3.24$), medial prefrontal (mPFC; −3/63/15; $z = 4.96$), lateral temporal cortices (LTC; left: −54/9/−30; $z = 4.99$; right: 42/15/−36; $z = 3.48$) and precentral gyrus/superior frontal gyrus/motor cortex. These effects are independent of any basic (360°) directional adaptation (images are exclusively masked by the effects of basic directional adaptation at threshold $P < 0.05$, uncorrected). **d**, The 60° adaptation effect is specific to fast runs. **e**, No significant adaptation is seen for fast running at 45° or 90° from the current direction. **f**, fMRI activity as a function of time since last fast run at 60° from the current direction ($\log[\text{time}]$ binned in quartiles), illustrating the adaptation effect. Signal in **d–f** is shown for the peak voxels in the four regions. All effects significant at $P < 0.001$, uncorrected; for display purposes, t -images are thresholded at $P < 0.000001$ in **a** and $P < 0.01$ in **c**. Error bars show mean and s.e.m. over participants.

well as spatial context^{3,4,25–27} for combination with parallel networks representing non-spatial information^{25,28–30}.

METHODS SUMMARY

Single-unit recording experiment in rats. Single-unit recordings were made from the medial entorhinal cortex of 17 male, Lister hooded rats, in accordance with appropriate Home Office Project and Personal licences. Each animal received a single microdrive carrying four tetrodes. While animals foraged for sweetened rice in a familiar environment, their positions and concomitant action potentials were captured using a standard procedure⁵. Grid cells were identified on the basis of their hexagonal spatial firing pattern, the regularity of which was assessed using a gridness measure^{1,5}. Post-recording, animals were killed, perfused with phosphate-buffered saline and then with 4% paraformaldehyde. Histology was conducted to confirm recording locations. See Methods and ref. 5 for details.

Functional neuroimaging experiment in humans. Forty-two male participants took part in this experiment (aged 18–31, mean age 23.1 years). The study was approved by the local Research Ethics Committee. Functional images were acquired on a 3T Siemens Allegra scanner using a gradient-echo echo-planar imaging (EPI) pulse sequence. Imaging data were analysed with SPM5 (<http://www.fil.ion.ucl.ac.uk/spm/>), including standard pre-processing procedures (spatial realignment, correction for differences in slice acquisition time, spatial normalization and smoothing) and modelling the data by a set of general linear models. During the virtual reality task, participants were presented with a first-person perspective of a grassy plane surrounded by a circular cliff. Participants moved the viewpoint by using their right hand to operate keys to move forward and turn left or right. Throughout the experiment, participants collected and replaced everyday objects within the arena. (See Methods and ref. 11 for details.)

Full Methods and any associated references are available in the online version of the paper at www.nature.com/nature.

Received 17 August; accepted 16 November 2009.

Published online 20 January 2010.

- Hafting, T., Fyhn, M., Molden, S., Moser, M. B. & Moser, E. I. Microstructure of a spatial map in the entorhinal cortex. *Nature* **436**, 801–806 (2005).
- McNaughton, B. L., Battaglia, F. P., Jensen, O., Moser, E. I. & Moser, M. B. Path integration and the neural basis of the 'cognitive map'. *Nature Rev. Neurosci.* **7**, 663–678 (2006).
- Burgess, N., Barry, C. & O'Keefe, J. An oscillatory interference model of grid cell firing. *Hippocampus* **17**, 801–812 (2007).
- Hasselmo, M. E. A model of episodic memory: mental time travel along encoded trajectories using grid cells. *Neurobiol. Learn. Mem.* **92**, 559–573 (2009).
- Barry, C., Hayman, R., Burgess, N. & Jeffery, K. J. Experience-dependent rescaling of entorhinal grids. *Nature Neurosci.* **10**, 682–684 (2007).
- Sargolini, F. et al. Conjunctive representation of position, direction, and velocity in entorhinal cortex. *Science* **312**, 758–762 (2006).
- Boccara, C. N. et al. Grid cells in presubiculum and parasubiculum. *FENS Abstr.* **4**, 128.21 (2008).
- Whitlock, J. R., Sutherland, R. J., Witter, M. P., Moser, M. B. & Moser, E. I. Navigating from hippocampus to parietal cortex. *Proc. Natl Acad. Sci. USA* **105**, 14755–14762 (2008).
- Logothetis, N. K. What we can do and what we cannot do with fMRI. *Nature* **453**, 869–878 (2008).
- Jeewajee, A., Barry, C., O'Keefe, J. & Burgess, N. Grid cells and theta as oscillatory interference: electrophysiological data from freely moving rats. *Hippocampus* **18**, 1175–1185 (2008).
- Doeller, C. F., King, J. A. & Burgess, N. Parallel striatal and hippocampal systems for landmarks and boundaries in spatial memory. *Proc. Natl Acad. Sci. USA* **105**, 5915–5920 (2008).
- Fernandez, G., Brewer, J. B., Zhao, Z., Glover, G. H. & Gabrieli, J. D. Level of sustained entorhinal activity at study correlates with subsequent cued-recall performance: a functional magnetic resonance imaging study with high acquisition rate. *Hippocampus* **9**, 35–44 (1999).
- Olsen, R. K. et al. Performance-related sustained and anticipatory activity in human medial temporal lobe during delayed match-to-sample. *J. Neurosci.* **29**, 11880–11890 (2009).
- Epstein, R., Graham, K. S. & Downing, P. E. Viewpoint-specific scene representations in human parahippocampal cortex. *Neuron* **37**, 865–876 (2003).
- Grill-Spector, K., Henson, R. & Martin, A. Repetition and the brain: neural models of stimulus-specific effects. *Trends Cogn. Sci.* **10**, 14–23 (2006).
- Park, S., Intrab, H., Yi, D. J., Widders, D. & Chun, M. M. Beyond the edges of a view: boundary extension in human scene-selective visual cortex. *Neuron* **54**, 335–342 (2007).
- Bakker, A., Kirwan, C. B., Miller, M. & Stark, C. E. Pattern separation in the human hippocampal CA3 and dentate gyrus. *Science* **319**, 1640–1642 (2008).
- Ekstrom, A. D. et al. Cellular networks underlying human spatial navigation. *Nature* **425**, 184–188 (2003).

19. Taube, J. S. Head direction cells and the neuropsychological basis for a sense of direction. *Prog. Neurobiol.* **55**, 225–256 (1998).
20. Chen, L. L., Lin, L. H., Green, E. J., Barnes, C. A. & McNaughton, B. L. Head-direction cells in the rat posterior cortex. I. Anatomical distribution and behavioral modulation. *Exp. Brain Res.* **101**, 8–23 (1994).
21. Byrne, P., Becker, S. & Burgess, N. Remembering the past and imagining the future: a neural model of spatial memory and imagery. *Psychol. Rev.* **114**, 340–375 (2007).
22. Wolbers, T., Wiener, J. M., Mallot, H. A. & Buchel, C. Differential recruitment of the hippocampus, medial prefrontal cortex, and the human motion complex during path integration in humans. *J. Neurosci.* **27**, 9408–9416 (2007).
23. Maguire, E. A. Neuroimaging studies of autobiographical event memory. *Phil. Trans. R. Soc. Lond. B* **356**, 1441–1451 (2001).
24. Schacter, D. L., Addis, D. R. & Buckner, R. L. Remembering the past to imagine the future: the prospective brain. *Nature Rev. Neurosci.* **8**, 657–661 (2007).
25. O'Keefe, J. & Nadel, L. *The Hippocampus as a Cognitive Map* (Oxford Univ. Press, 1978).
26. Howard, M. W., Fotedar, M. S., Datey, A. V. & Hasselmo, M. E. The temporal context model in spatial navigation and relational learning: toward a common explanation of medial temporal lobe function across domains. *Psychol. Rev.* **112**, 75–116 (2005).
27. Pastalkova, E., Itskov, V., Amarasingham, A. & Buzsaki, G. Internally generated cell assembly sequences in the rat hippocampus. *Science* **321**, 1322–1327 (2008).
28. Gaffan, D. Scene-specific memory for objects: a model of episodic memory impairment in monkeys with fornix transection. *J. Cogn. Neurosci.* **6**, 305–320 (1994).
29. Knierim, J. J. Neural representations of location outside the hippocampus. *Learn. Mem.* **13**, 405–415 (2006).
30. Eichenbaum, H., Yonelinas, A. P. & Ranganath, C. The medial temporal lobe and recognition memory. *Annu. Rev. Neurosci.* **30**, 123–152 (2007).

Supplementary Information is linked to the online version of the paper at www.nature.com/nature.

Acknowledgements We acknowledge K. Jeffery and J. O'Keefe for providing help and facilities for single-unit recording; the Wellcome Trust Centre for Neuroimaging at UCL for providing help and scanning facilities; J. Krupic and R. Hayman for help with single-unit data collection; A. Jeewajee for help with analyses; J. King for help with virtual reality programming; and useful discussions with P. Dayan, K. Friston, U. Frith, C. Hall, A. Jeewajee, J. O'Keefe and M. Witter. This work was funded by the UK Medical Research Council and the European Union (SpaceBrain grant).

Author Contributions C.F.D., C.B. and N.B. jointly conceived and designed the experiments. C.F.D. performed the fMRI experiment and data analyses; C.B. performed the single-unit experiment and data analyses; N.B. gave direction on analyses; all authors discussed the analyses and results and contributed to writing the paper.

Author Information Reprints and permissions information is available at www.nature.com/reprints. The authors declare no competing financial interests. Correspondence and requests for materials should be addressed to C.F.D. (c.doeller@ucl.ac.uk) or N.B. (n.burgess@ucl.ac.uk).

METHODS

Single-unit recording experiment in rats: animals and surgery. Seventeen male Lister hooded rats (250–400 g at implantation) each received a single microdrive carrying four tetrodes³¹ of twisted 17–25 µm HM-L coated platinum-iridium wire (90–10%) (California Fine Wire). In most cases 17 µm wire was platinum plated to reduce impedance to 200–300 kΩ at 1 kHz. The surgical procedure and housing conditions were the same as those described previously⁵. All work was conducted within the terms of appropriate Home Office Project and Personal licences.

Recording and behavioural training. Training and screening was performed post-surgically after a 1 week recovery period. An Axona recording system was used to acquire the single unit and positional data (see ref. 5 for details). The position of the rat was captured using an overhead video camera to record the position of the one or two LEDs on the animal's head-stage. In all cases head direction was inferred from the animal's trajectory. Animals were trained to forage for sweetened rice in a 1 m by 1 m square environment. Environment floors were made of either Perspex or polyvinyl and were wiped down with water between trials. Training consisted of at least three trials, each in excess of 15 min, distributed over 3 days. After this period animals would run continuously as they searched for sweetened rice. Activity was recorded while the animals foraged in the now familiar environment, with the exception of three rats trained in a 110-cm diameter cylinder and tested in 110-cm or 100-cm cylinders. In all cases the laboratory was visible above the arena wall. All recording trials were 20 min long. On days in which multiple recording trials were made only a single trial, usually the first, was used. The winding protocol, spatial firing correlates, and spike amplitudes were used to exclude multiple recordings of the same cell such that only the first recording was used. Potential grid cells were selected visually by the experimenter on the basis that they exhibited the regular triangular firing pattern diagnostic of grid cells. In this way 140 cells were subject to further analysis.

Data analysis: spike sorting and binning. Spike sorting was performed offline using a data analysis suite (Tint, Axona) and using Matlab (Mathworks). Action potentials were assigned to potential cells based on amplitude, waveform and temporal autocorrelation criteria applied elsewhere to entorhinal grid cells^{1,5}. The animal's position and spike locations were binned into a 64 × 64 bin array covering the camera's field of view; each bin being the equivalent of 8 × 8 pixels, roughly 2 × 2 cm. Unsmoothed rate maps were calculated by dividing the number of spikes assigned to a bin by the cumulative occupancy of the bin. For smoothed rate maps the firing rate for bin i was the number of spikes in a 5 × 5 kernel centred on i divided by the cumulative occupancy of the same bins. Similarly, polar rate maps were constructed using 6 degree radial bins and were smoothed with a Gaussian kernel ($\sigma = 10^\circ$).

Gridness and grid orientation. Spatial autocorrelograms were estimated from unsmoothed rate maps^{1,6}, smoothed (using a two-dimensional Gaussian kernel, $\sigma = 2.5$ bins), and used to assess the periodicity, regularity and orientation of cells with multiple firing fields. The spatial autocorrelogram was defined as:

$$r(\tau_x, \tau_y) = \frac{n \sum \lambda_1(x, y) \lambda_2(x - \tau_x, y - \tau_y) - \sum \lambda_1(x, y) \sum \lambda_2(x - \tau_x, y - \tau_y)}{\sqrt{n \sum \lambda_1(x, y)^2 - (\sum \lambda_1(x, y))^2} \sqrt{n \sum \lambda_2(x - \tau_x, y - \tau_y)^2 - (\sum \lambda_2(x - \tau_x, y - \tau_y))^2}}$$

where $r(\tau_x, \tau_y)$ is the autocorrelation between bins with spatial offset of τ_x and τ_y , $\lambda_1(x, y)$ and $\lambda_2(x, y)$ are the mean firing rate in bin (x, y) of the firing rate map and n is the number of pairs of visited bins. Six 'central peaks' were identified as the local maxima closest to, but excluding, the central peak in the spatial autocorrelogram. The extent of each peak was defined as the contiguous set of bins around the peak with a value greater than half the peak value. The orientation of each cell was calculated as the angle between a nominal east reference line and an axis defined by the centre of the spatial autocorrelogram and the peak closest to the reference line in an anticlockwise direction from east. Gridness, a measure of spatial periodicity, was calculated by defining an area of the spatial autocorrelogram centred on but excluding the central peak bounded by a circle passing around the outermost edge of the six central peaks. This area was rotated in 30° increments up to 150°, and for each rotation the correlation coefficient with the un-rotated area was found. Gridness was defined as the lowest correlation for rotations of 60° and 120° minus the highest correlation for 30°, 90° or 150°. Cells with gridness of 0 or greater were classified as grid cells (see Supplementary Fig. 6). A total of 113 cells from 16 of the 17 rats were judged to be grid cells.

Directionality and directional measures. The directionality of firing exhibited by each grid cell was defined as the KL divergence between the polar rate map and a uniform circular distribution with equal mean:

$$D_{KL} = \sum_i \frac{\tau_1(i) \log(\tau_1(i))}{\tau_2(i)}$$

where $\tau_1(i)$ is the value in the i th bin of a polar rate map normalized to have area 1 and $\tau_2(i)$ is the value in the i th bin of a uniform probability distribution with the

same number of bins as τ_1 . Cells with $D_{KL} \geq 0.15$ were considered directional, consistent with the experimenter's intuition, producing a total of 18 directional cells from 8 rats (see Supplementary Figs 3–6). For each directional grid cell the circular mean of the polar rate map was calculated according to:

$$\mu_{\text{circ}} = \arctan \left(\frac{\sum_i \tau_1(i) \sin \theta_i}{\sum_i \tau_1(i) \cos \theta_i} \right)$$

Where θ_i is the angle of the centre of radial bin i and $\tau_1(i)$ is defined above.

Histology. After the experiment rats received an overdose of Euthatal (sodium pentobarbital) and were transcardially perfused with phosphate-buffered saline and then with 4% paraformaldehyde (PFA) solution. The brains were removed and stored in 4% PFA for at least 1 week before sectioning (in some cases 20% sucrose cryo-protection was used). 40 µm frozen sagittal sections were cut, mounted on gelatine-coated glass slides and stained with cresyl violet. High resolution images were acquired using either an Olympus microscope with Xli digital camera (XL Imaging Ltd.) or Nikon Labophot-2 microscope with Leica DFC420c camera. The depth and layer at which cells were recorded was extrapolated from the record of tetrode movements after taking account of brain shrinkage. All recordings were confirmed to the dorso-lateral extent of the medial entorhinal cortex (see Supplementary Fig. 2 for examples of recording locations).

Functional neuroimaging experiment in humans: participants. Forty-two male participants took part in this experiment (aged 18–31, mean age 23.1 years). Participants gave written consent and were paid for participating, as approved by the local Research Ethics Committee. All were right-handed with normal or corrected-to-normal vision and reported to be in good health with no history of neurological disease. All had previous experience of playing first person perspective video games. The current report includes data from a previous study¹¹ where we report the results of unrelated analyses.

Virtual reality environment and task. We used UnrealEngine2 Runtime software (Epic Games) to present a first-person perspective view of a grassy plane surrounded by a circular cliff with a background of mountains, clouds and the sun (created using Terragen, Planetside Software) projected at infinity, to provide orientation but not location within the arena. One rotationally symmetric intramaze landmark was always present in the arena. Participants moved the viewpoint by using their right hand to operate keys to move forward and turn left or right. The viewpoint is ~2 virtual metres above ground, the arena is ~180 virtual metres in diameter and the virtual heading and location were recorded every 100 ms. Participants received training in an unrelated virtual environment before performing the experiment and then familiarized themselves with the main arena in the scanner. Throughout the experiment, participants collected and replaced everyday objects within the arena. They collected each object once during an initial trial, by running over it. In each subsequent trial they saw an image of one of the objects and had to move to where they thought the object had been in the arena. After their response by a button press, feedback was provided (that is, the object appeared in its correct position and participants collected it again). Memory was measured in terms of the proximity of the replace response location to the correct object location (see Supplementary Fig. 7 and ref. 11).

fMRI acquisition. Blood-oxygenation-level-dependent (BOLD) T2*-weighted functional images were acquired on a 3T Siemens Allegra scanner using a gradient-echo echo-planar imaging (EPI) pulse sequence with the following parameters: Repetition time (TR) = 2,600 ms, echo time (TE) = 30 ms, flip angle = 90°, slice thickness = 2 mm, interslice gap = 1 mm, in-plane resolution = 3 × 3 mm, field of view (FoV) = 192 mm², 40 slices per volume. The first five volumes were discarded to allow for T1 equilibration. The sequence was optimized to minimize signal dropouts in the medial temporal lobes³². In addition, a field map using a double echo FLASH sequence was recorded for distortion correction of the acquired EPI images³² (see below). For 32 of the participants we also acquired a standard T1-weighted structural MRI scan (3D MDEFT, resolution = 1 × 1 × 1 mm).

Image pre-processing. The main imaging analyses were performed with SPM5 (<http://www.fil.ion.ucl.ac.uk/spm/>) within Matlab. Additional analyses were conducted outside SPM using Matlab. Functional images were spatially realigned to the first image in the times series, were corrected for distortions based on the field map³³ and the interaction of motion and distortion using the Unwarp routines in SPM^{33,34}, and sinc-interpolated in time to correct for differences in slice acquisition time. The structural images underwent segmentation (into grey matter, white matter and cerebro-spinal fluid), bias correction and spatial normalization to the MNI template using 'unified segmentation'³⁵. For participants with a structural scan, functional images were normalized based on the spatial parameters derived from the normalization of their structural images. For participants without a structural scan, images were normalized to an EPI template specific to our sequence and scanner that was aligned to the MNI T1 template.

Finally, the normalized functional images were spatially smoothed with an isotropic 8-mm full-width-half-maximum Gaussian kernel.

Analysis of fMRI time series. After pre-processing, fMRI time series were modelled by a set of general linear models (GLMs). All models included regressors for the entire time of virtual reality navigation, separated by the participant's speed of movement (three equal tertiles for high, medium and slow speed), various parametric modulations of these regressors (see details below), and regressors of no interest modelling phases without navigation in the environment (see ref. 11). All parametric modulations are normalized to have zero mean and thus be orthogonal to the un-modulated regressor³⁶. All regressors (parametrically modulated or not) were convolved with the canonical haemodynamic response function (HRF) in SPM before entering the GLM. Data were high-pass filtered at 1/128 Hz. Coefficients for each regressor were estimated for each participant using maximum likelihood estimates to account for serial correlations in the data. Linear contrasts of coefficients for each participant were entered into second level random-effects analyses. The statistical reliability (across participants) of differences of parameter estimates from each other, or from zero, are shown and referred to as fMRI 'activation'. On the basis of our strong a priori hypotheses we have chosen an uncorrected statistical threshold of $P < 0.001$ for whole-brain analyses. Analyses of single comparisons (for example, concerning the mean activation across an ROI) are tested at $P = 0.05$. Coordinates of brain regions are reported in MNI space.

Entorhinal cortex ROI. We defined an ROI including both entorhinal cortices following anatomical boundaries as described previously³⁷. In rats, grid cells are found in the medial but not the lateral entorhinal cortex. However, the homologues of these subdivisions in humans are not known. Eight subdivisions of the human entorhinal cortex have been identified³⁸. The medio-lateral orientation of most of these subdivisions rules out a simple correspondence between medial entorhinal areas in humans and medial entorhinal cortex in rodents. In rats, medial entorhinal cortex receives direct input from presubiculum. In monkeys, the more posterior subdivisions of entorhinal cortex receive such input (M. Witter, personal communication), which might also be the case in humans. We note that many, but not all, of our entorhinal cortex activations are more posterior, and that the coherence of potential grid orientation is slightly stronger in posterior than anterior entorhinal cortex. However, future high-resolution imaging in humans and anatomical studies in non-human primates will be required to resolve this issue fully.

Quadrature filter and mean grid orientation analysis. To estimate the potential grid orientations in entorhinal cortex, we used a quadrature filter, a well-known signal processing technique, on one-half of the data. We separated each participant's virtual navigation fMRI data arbitrarily into 12 scanning runs of equal length. For one-half of the data (odd runs), we calculated the cosine and sine of the participant's virtual running direction $\theta(t)$ with a periodicity of 60° , that is, $\cos(6\theta(t))$ and $\sin(6\theta(t))$, arbitrarily aligned to 0° of the virtual reality environment as defined by the background cues (see Supplementary Fig. 8) separately for fast, medium and slow runs. The factor 6 means that these regressors are sensitive to activation showing a six-fold rotational symmetry in running direction (that is, activation with six evenly spaced peaks as a function of running direction will produce parameter estimates for the two regressors (β_1 and β_2)

with large amplitude ($\sqrt{\beta_1^2 + \beta_2^2}$). These cosine and sine regressors (separately for the three speed levels) were included in the GLM used to analyse the fMRI data. The resulting parameter estimates β_1 and β_2 were used to calculate the potential grid orientation in each voxel Φ (varying between 0 and 59°) in the entorhinal ROI as $\Phi = [\arctan(\beta_2/\beta_1)]/6$, where \arctan is mapped into the range $[0-360^\circ]$ according to the signs of β_2 and β_1 , separately for the three speed levels. The 'mean grid orientation' for the region (φ) was defined as the population vector (vector average of grid orientations Φ in each voxel weighted by the amplitude of sinusoidal modulation in that voxel, or $[\arctan(<\beta_2>/<\beta_1>)]/6$ where $<>$ denotes the mean across voxels), separately for the three speed levels.

In a next step, we looked for sinusoidal modulation of activation with six-fold rotational symmetry in the other half of the data (even runs). We conducted the following analyses: (1) calculating the six-fold cosine of the direction of virtual navigation aligned to the mean grid orientation (that is, $\cos\{6[\theta(t)-\varphi]\}$) resulting in one aligned cosine parametric regressor per speed level (see Fig. 3 and Supplementary Fig. 8). (2) For visualization of the effect, we separated runs aligned (within 15° of the nearest main axis of the grid) from those misaligned to the main grid axes (more than 15° from a grid axis), resulting in two (aligned versus misaligned) non-parametric regressors per speed level (see Fig. 3 and Supplementary Fig. 10).

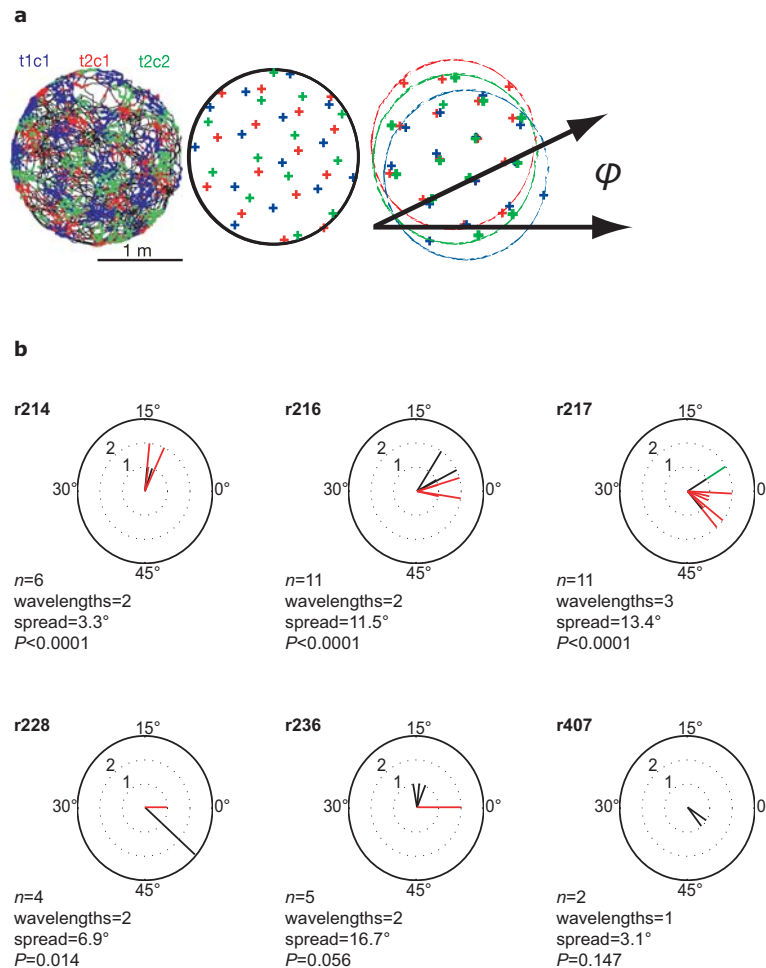
Control models. To test for the specificity of the six-fold symmetric sinusoidal modulation, we used the same approach of (1) estimating the mean grid orientation of entorhinal cortex and (2) looking for sinusoidal modulation in control models, however with directional periodicities of 90° and 45° (that is, four-fold and eight-fold rotational symmetry; Fig. 3) and of 72° and 51.4° (that is, five-fold and seven-fold rotational symmetry) respectively (see Supplementary Fig. 11).

Adaptation analyses. In the basic analysis of adaptation to running direction we separated the whole directional range of the participant's virtual path into 36 equal 10° bins and then looked for fMRI correlates of how recently participants were running in the current direction bin (regressor: $\log[\text{time since last running in the current direction}]$), separately for the three speed levels. To make sure that the adaptation effect is not confounded by angular velocity, the model also included a regressor reflecting angular velocity. In a next step we used the same logic as the above analysis but looked for adaptation to running directions shifted by 60° from the current direction (regressor: $\log[\text{time since last running at } 60^\circ \text{ to the current direction}]$). For the visualization of the adaptation effect, we grouped trials into four bins reflecting quartiles of the $\log[\text{time}]$ regressor, estimated a new GLM, and calculated the per cent signal change separately for each bin. (See bar plots in Fig. 4f.) We also analysed control models, with adaptation to directions shifted by 90° and 45° from the current direction (regressor: $\log[\text{time since last running at } 90^\circ \text{ and } 45^\circ \text{ to the current direction}]$).

Showing fMRI effect sizes. The mean fMRI signal is expressed in terms of per cent signal change compared to the 'baseline' level of fMRI activation (the constant term in the GLM, changes from which are modelled by our regressors) for the peak voxel in a region found in the respective analyses and averaged across participants. The adaptation effect is also expressed as per cent signal change: the amplitude of the adaptation regressor fitted by the GLM (that is, the difference between the amplitude of response when the previous sample was most recent versus longest ago) compared to the baseline level. In our analyses 'sample' corresponds to running in the current direction (Fig. 4a, b) or $\pm 60^\circ$ from it (Fig. 4c, d).

31. Recce, M. & O'Keefe, J. The tetrad: a new technique for multiunit extracellular recording. *Soc. Neurosci. Abstr.* 15, 1250 (1989).
32. Weiskopf, N., Hutton, C., Josephs, O. & Deichmann, R. Optimal EPI parameters for reduction of susceptibility-induced BOLD sensitivity losses: a whole-brain analysis at 3 T and 1.5 T. *Neuroimage* 33, 493–504 (2006).
33. Hutton, C. et al. Image distortion correction in fMRI: A quantitative evaluation. *Neuroimage* 16, 217–240 (2002).
34. Andersson, J. L., Hutton, C., Ashburner, J., Turner, R. & Friston, K. Modeling geometric deformations in EPI time series. *Neuroimage* 13, 903–919 (2001).
35. Ashburner, J. & Friston, K. J. Unified segmentation. *Neuroimage* 26, 839–851 (2005).
36. Büchel, C., Holmes, A. P., Rees, G. & Friston, K. J. Characterizing stimulus-response functions using nonlinear regressors in parametric fMRI experiments. *Neuroimage* 8, 140–148 (1998).
37. Fischl, B. et al. Predicting the location of entorhinal cortex from MRI. *Neuroimage* 47, 8–17 (2009).
38. Insausti, R., Tunon, T., Sobreviela, T., Insausti, A. M. & Gonzalo, L. M. The human entorhinal cortex: a cytoarchitectonic analysis. *J. Comp. Neurol.* 355, 171–198 (1995).

SUPPLEMENTARY INFORMATION

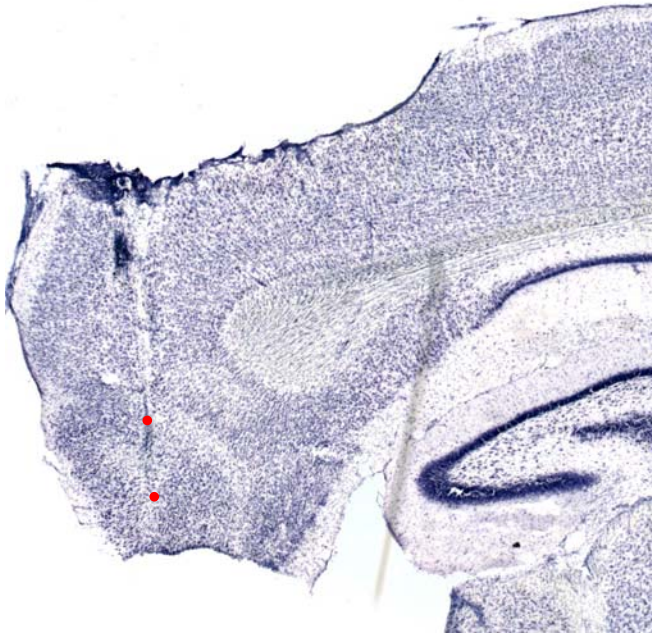


Supplementary Figure 1 | Grids from different grid cells have a common orientation. a, Grid cells recorded from similar dorso-ventral locations have grid-like firing patterns with similar spatial scale and orientation (ϕ), see Hafting et al, Nature 2005 (ref. 1). Left: The firing locations of three grid cells simultaneously recorded on two tetrodes are shown in red, green and blue respectively. Middle: the locations of the grid nodes show the three grids to have similar orientation and scale, so that they align when displaced appropriately (Right). Adapted from Hafting et al, Nature 2005, Figure 3, with permission. **b**, Grid cells recorded from the same rat over a wider range of locations and recording sessions have grids with similar orientations, even though their spatial scale varies. Grid cells from six rats were analysed for their orientation (as shown in Supplementary Fig. 3) by Barry et al, Nat Neurosci 2007 (ref. 5). For each rat the orientation of the grids is shown on a circular plot representing angles between 0° and 59° such that 0° = 60°. A cell is represented by a line of length 1, additional cells with the same orientation extend that line. Grids that differed in spatial scale by less than 20% were grouped; each group is coloured differently. The number of cells, number of distinct spacing-groups and angular distance (spread) between the most disparately oriented cells is shown. *P* values are for the Rayleigh test of circular non-uniformity; the first four rats show significant clustering of orientations. Grids with similar spacing may be part of a local recurrent circuit and so might not represent independent data points. To mitigate this, the mean orientation of each spacing-group was found and the spread between groups in the same rat calculated. Spread, pooled across rats, was found to depart significantly from circularity (Rayleigh test, $P = 0.002$), suggesting that in the same rat even grids with different wavelengths share similar orientations. Adapted from Barry et al, Nat Neurosci 2007, Figure S4, with permission.

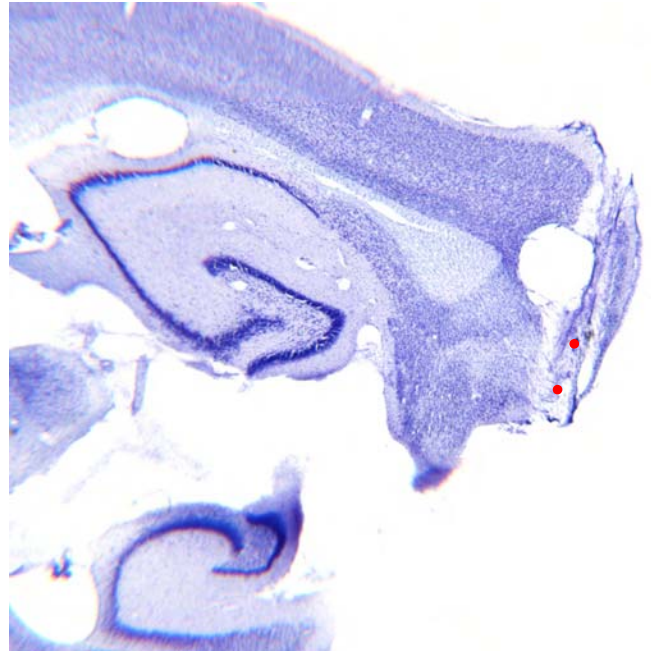
Rat	No. grid cells (gridness ≥ 0)	No. directional grid cells (gridness ≥ 0 & KL div ≥ 0.15)
214	7	4
216	11	3
217	16	3
1445	17	3
1457	15	2
1494	10	0
1538	0	0
1549	2	0
1597	1	0
1598	9	0
1599	1	0
1603	1	1
1604	2	0
1618	1	1
1625	12	1
1635	5	0
1649	3	0
Total	113	18

Supplementary Figure 2 | Recording locations. a, Distribution of grid cells between animals. **b,** on next page: Cresyl violet stained sagittal sections showing typical recording location for four rats. Recording locations (inferred from tracks and winding protocol) are as follows: r217 MEC layer III; r1625 MEC layer II/III; r1597 MEC layer III; r1445 MEC layer III moving into II. Red dots indicate the range over which grid cells were recorded.

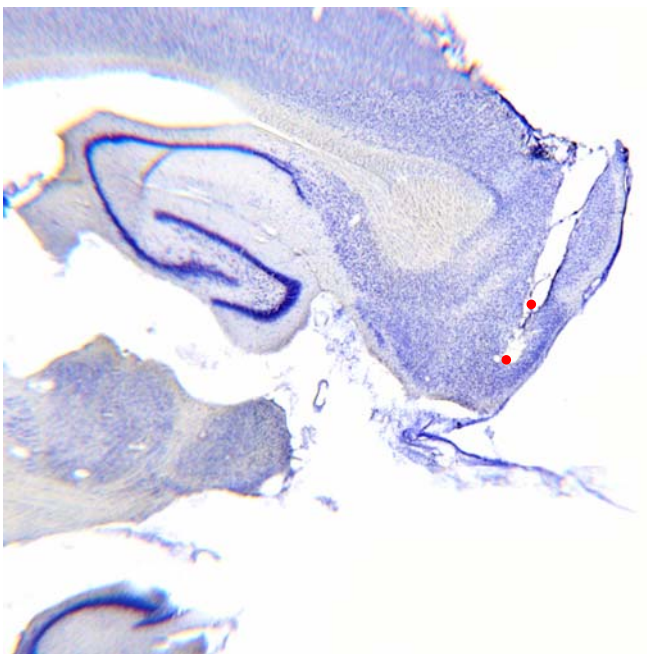
r217



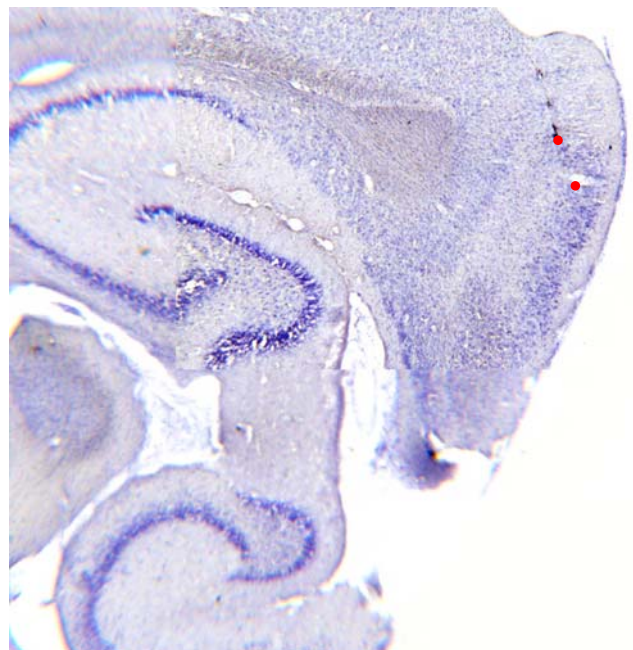
r1625

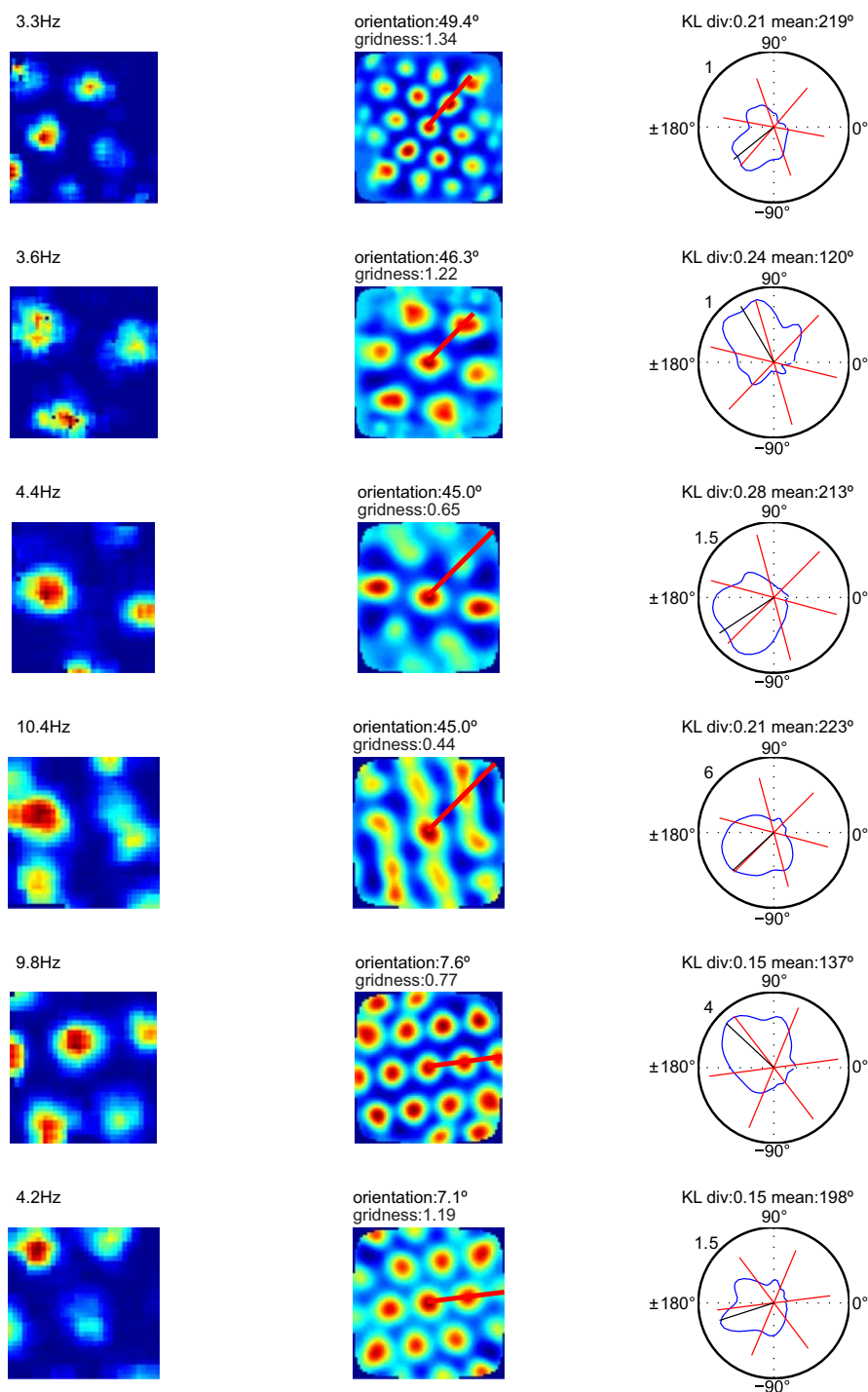


r1597

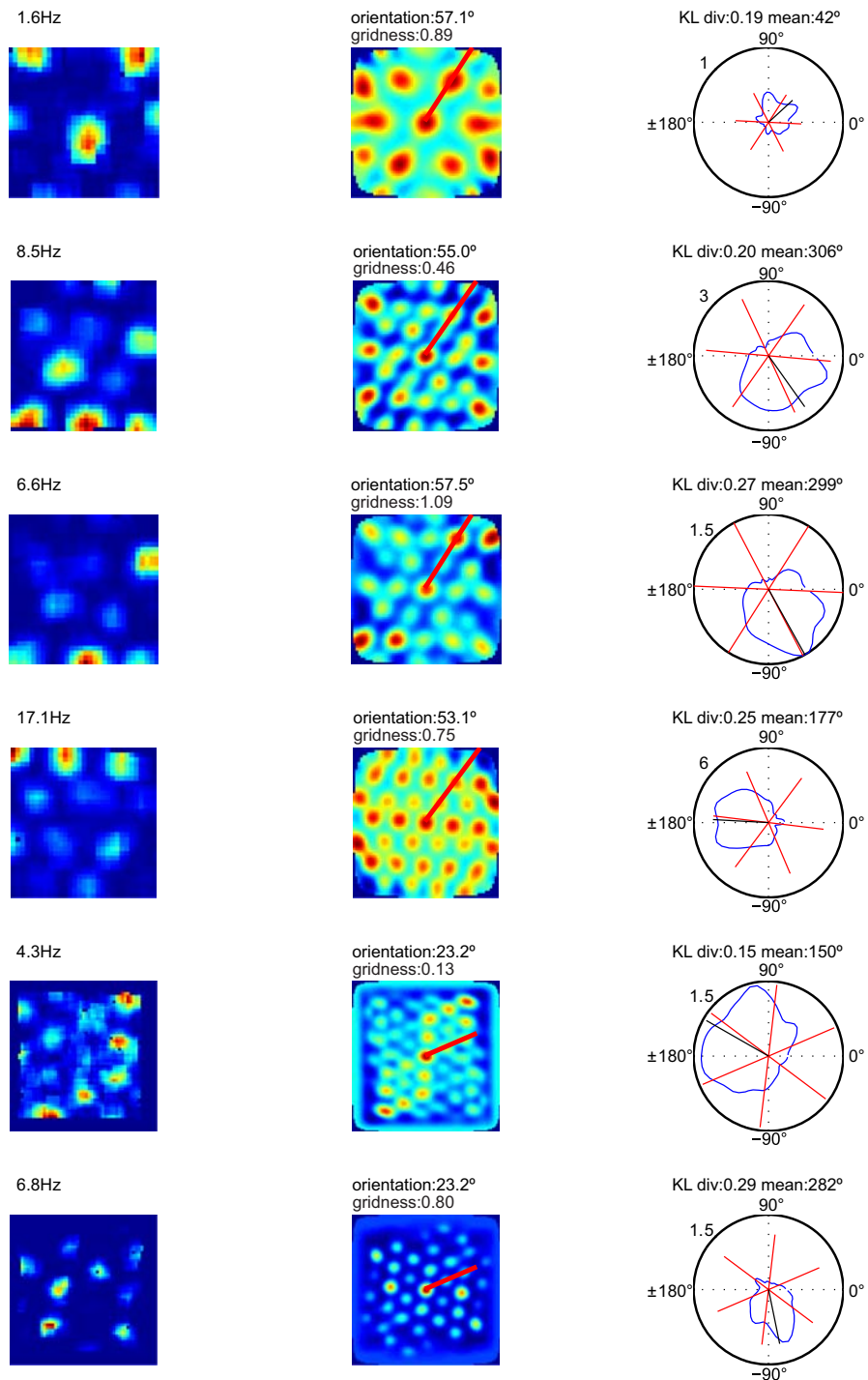


r1445

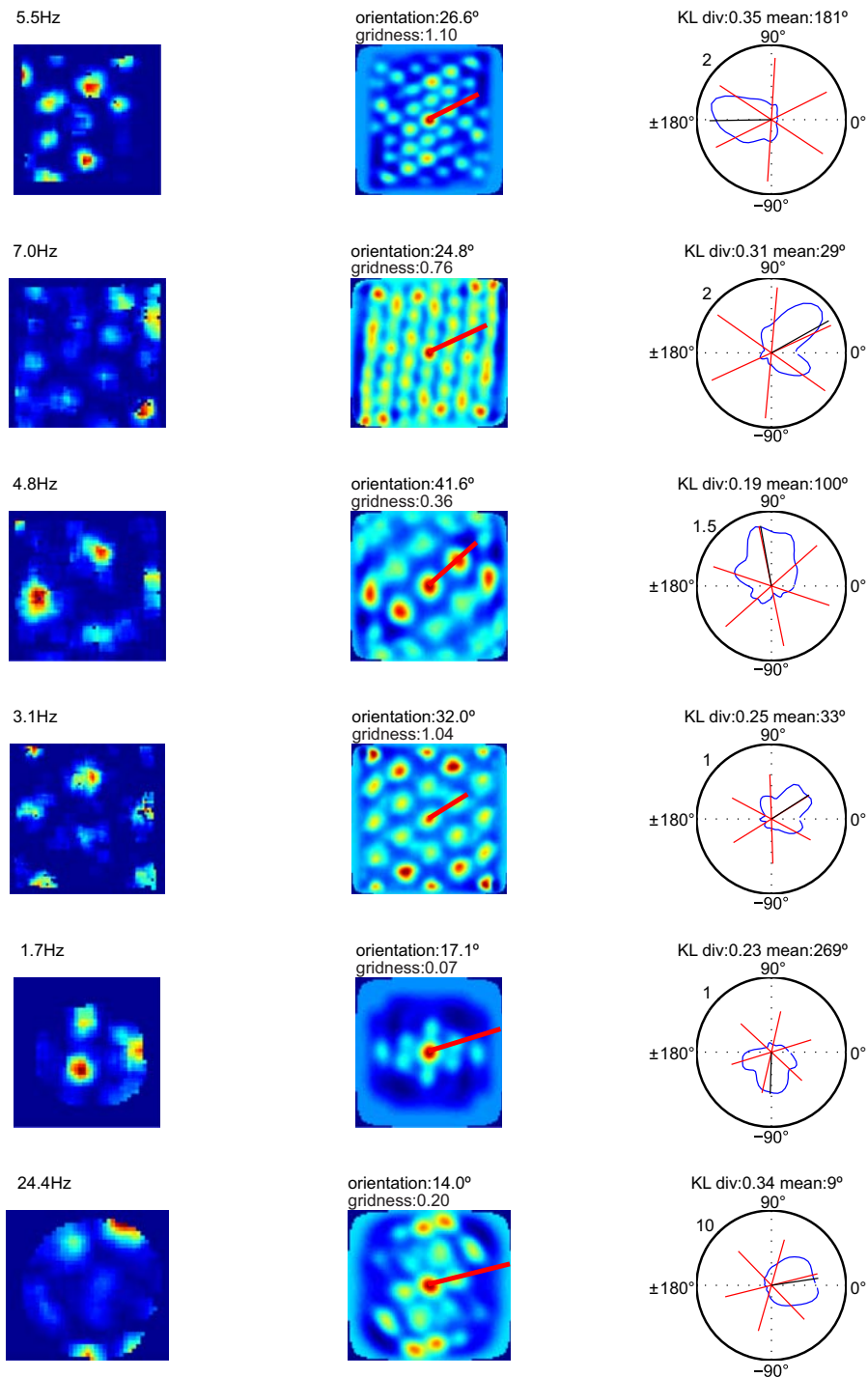




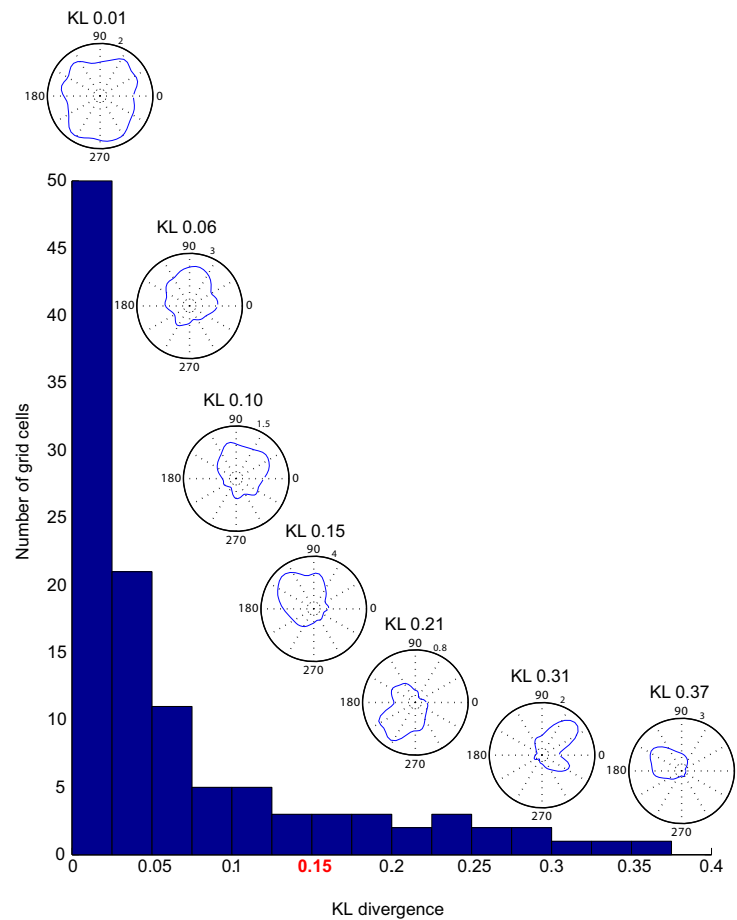
Supplementary Figure 3, part 1 | Locational and directional firing rate maps, and spatial autocorrelograms for all directional grid cells ($n=18$). Left, ratemap showing firing rate as a function of the rat's location (red: high firing rate, blue: low rate, value above map is the maximum firing rate). Centre, spatial autocorrelogram constructed from the positional ratemap. Red line indicates the orientation of the grid-like firing pattern (orientation is displayed above the plot in degrees along with gridness). Right, polar firing ratemap. Black line indicates mean firing direction and red lines indicate the main axes of the grid firing pattern identified from the spatial autocorrelogram. The KL divergence and mean firing direction for each cell is listed above the polar plot. Figure continues on the next 2 pages.



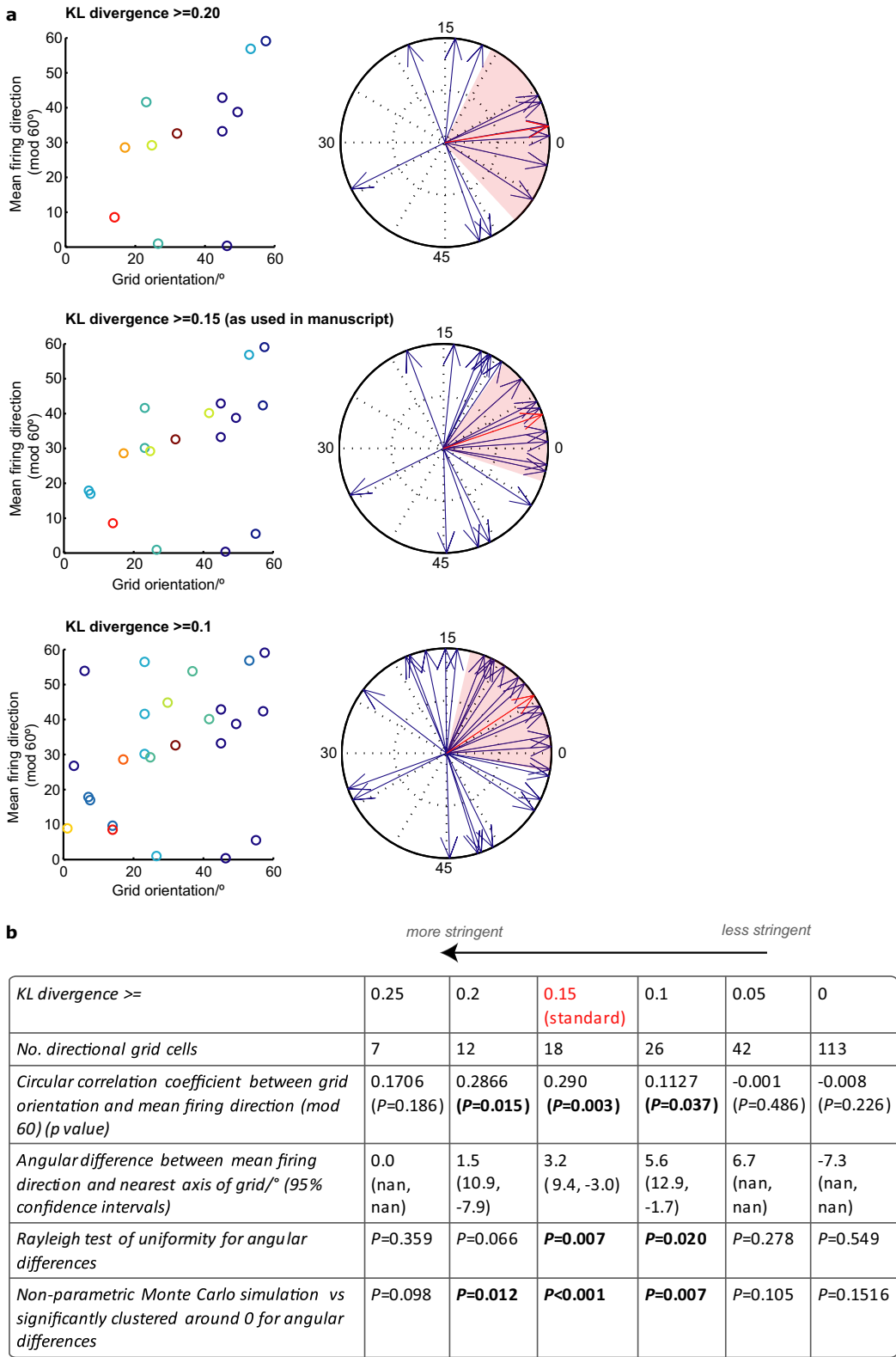
Supplementary Figure 3, part 2



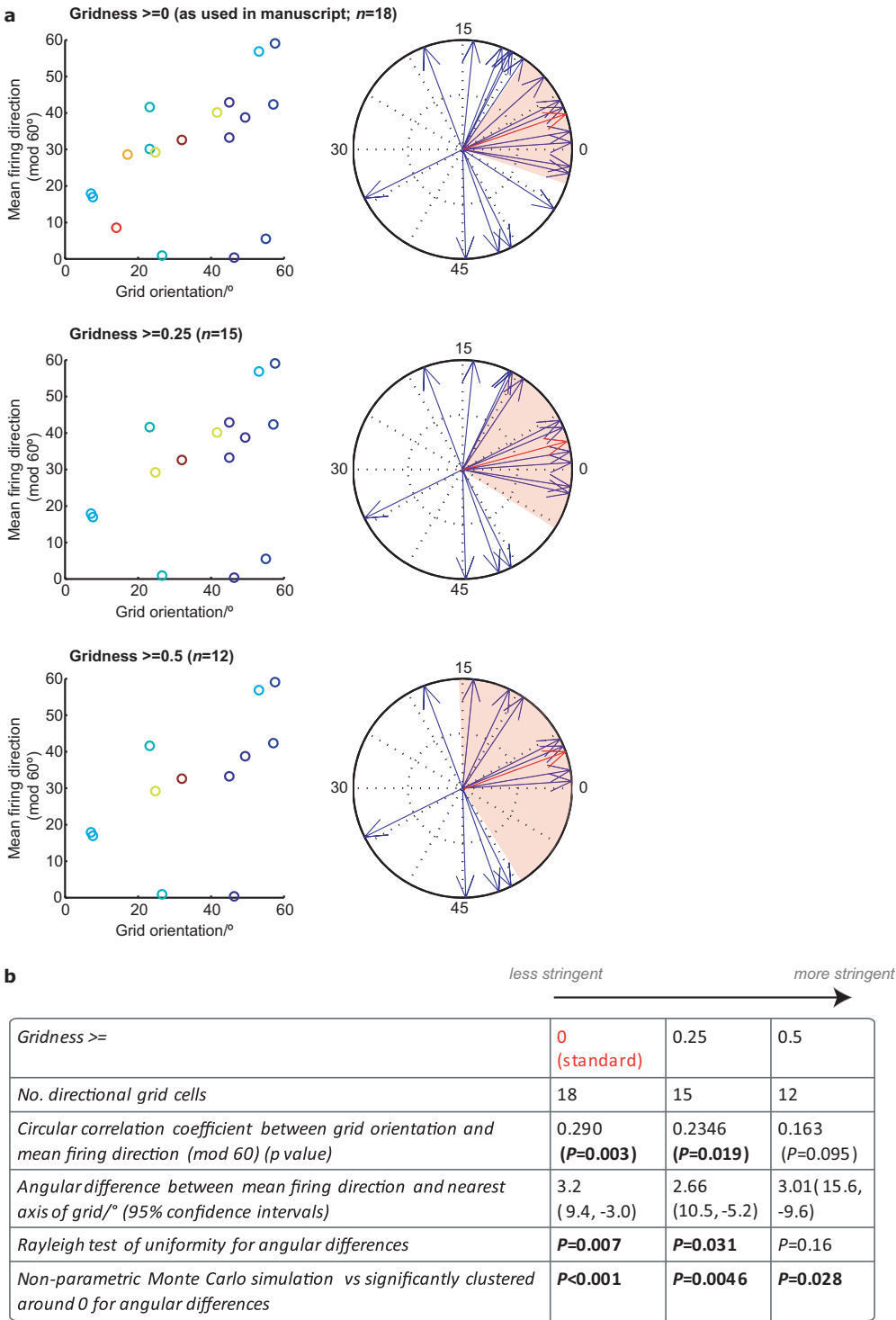
Supplementary Figure 3, part 3



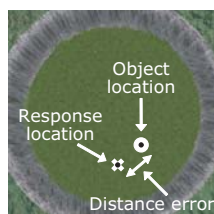
Supplementary Figure 4 | Distribution of directional KL divergence for all grid cells ($n=113$). The KL divergence between the directional ratemap of each grid cell and a uniform distribution with equal mean was used to assess how directional the firing of each cell was; cells with KL divergence ≥ 0.15 were considered to be directional grid cells ($n=18$). The histogram shows the number of grid cells present in the population for each level of KL divergence. Polar plots show directional ratemaps typical of the illustrated KL level.



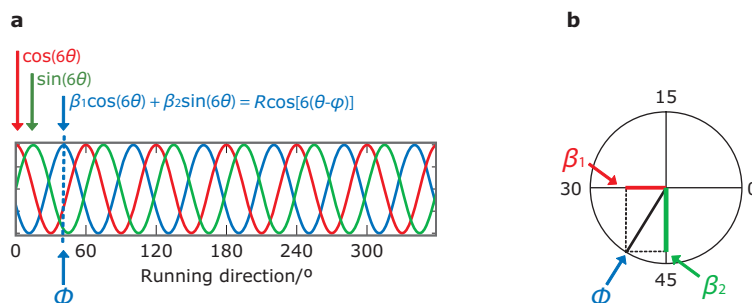
Supplementary Figure 5 | Mean firing directions of directional grid cells are aligned to the grid and this effect is robust to a variety of directionality criteria. **a**, Left, Scatter plots of all directional grid cells showing grid orientation vs. mean firing direction, modulo 60° . Right, Angular difference between the mean firing direction of each cell and the nearest axis of its grid-like firing pattern, red arrows show the mean difference and the red shaded area indicates 95% confidence intervals. Plots are shown for grid cells selected at three different levels of directionality criteria: top, grid cells with directional firing that equals or exceeds KL divergence 0.20 (i.e. very directional cells, $n=12$); middle, grid cells with $KL \geq 0.15$ (i.e. the value used in the manuscript, $n=18$); bottom, cells with $KL \geq 0.10$ (i.e. including less directionally-modulated grid cells, $n=26$). **b**, Table of statistical results for tests applied to cells selected at six different levels of directionality criteria ranging from $KL \geq 0.25$ (i.e. highly directional grid cells) to $KL \geq 0$ (i.e. all grid cells). Significance is high when the criteria is low enough to allow a large sample (e.g., $KL \leq 0.2$) and high enough to exclude non-directional cells (e.g., $KL \geq 0.1$).



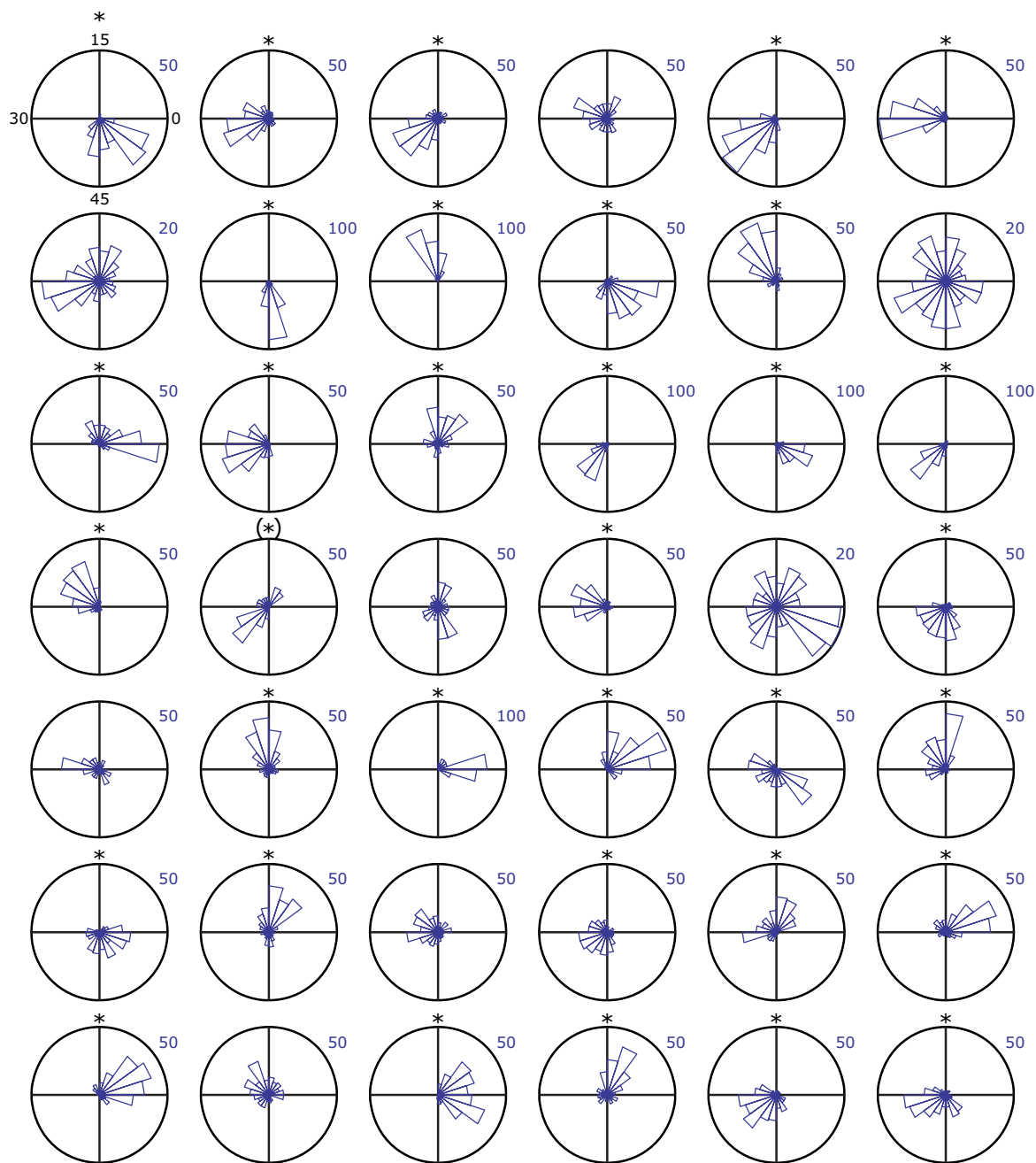
Supplementary Figure 6 | Mean firing directions of directional grid cells are aligned to the grid and this effect is robust to a variety of gridness criteria. **a**, Left, scatter plots of all directional grid cells showing grid orientation vs. mean firing direction, modulo 60° . Right, angular difference between the mean firing direction of each cell and the nearest axis of its grid-like firing pattern, red arrows show the mean difference and the red shaded area indicates 95% confidence intervals. Plots are shown for grid cells selected at three different levels of gridness criteria (NB directional criterium is KL divergence ≥ 0.15 in all cases): top, grid cells with gridness that equals or exceeds 0 (i.e. the value used in the manuscript; $n=18$); middle, grid cells with gridness ≥ 0.25 (i.e. excludes the least regular grids from the previous plot; $n=15$); bottom, grid cells with gridness ≥ 0.5 (i.e. only the most regular grids; $n=12$). **b**, Table of statistical results for tests applied to cells selected at three different levels of gridness criteria ranging from gridness ≥ 0 (i.e. all grid cells) to gridness ≥ 0.5 (i.e. only the very most regular grid cells).



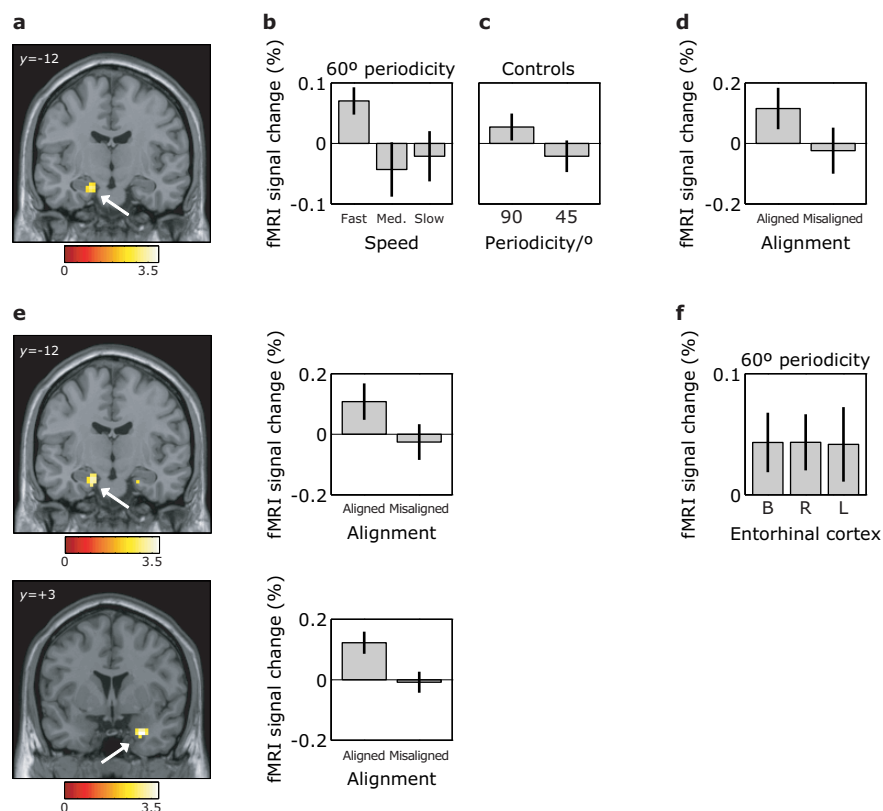
Supplementary Figure 7 | Measuring spatial memory. Participants collected and replaced objects found within the arena, see Methods and ref. 11 for details. Inaccuracy (error) was measured as the distance between the replace response location (indicated by a white 'x') and the correct object location (indicated by a white dot), in virtual metres. Each participant's spatial memory performance was measured as the inverse of their mean distance error.



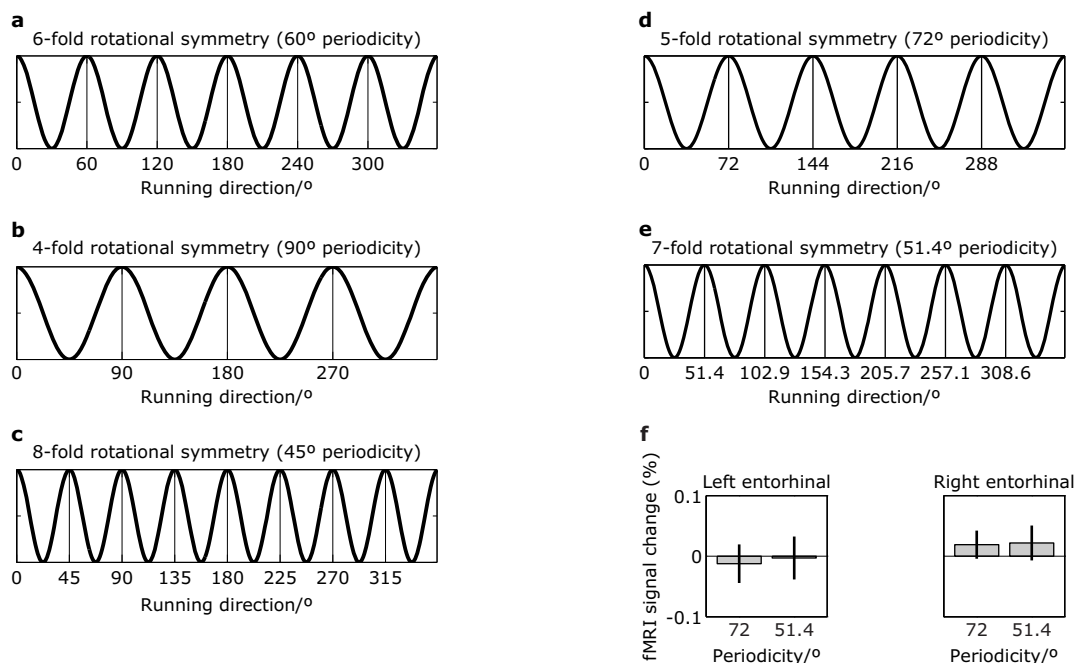
Supplementary Figure 8 | Quadrature filter analysis of mean grid orientation. **a**, We calculated the 6-fold symmetric cosine (red) and sine (green) of each participant's virtual running direction $\theta(t)$, i.e., cosine and sine with directional periodicity of 60° , $\cos(6\theta(t))$ and $\sin(6\theta(t))$. These were convolved with the hemodynamic response function and fitted to one half of the fMRI data as two regressors in a GLM. **b**, The resulting regression coefficients β_1 and β_2 were then used to calculate the potential grid orientation for each voxel (ϕ , varying between 0 and 59°) as $\phi = [\arctan(\beta_2/\beta_1)]/6$, where \arctan is mapped into the range $[0-360]$ according to the signs of β_2 and β_1 . See illustration. The 'mean grid orientation' for the ROI (ϕ) was defined as the population vector (the vector average of grid orientations ϕ weighted by amplitude, or $[\arctan(\langle\beta_2\rangle/\langle\beta_1\rangle)]/6$ where $\langle\rangle$ denotes the mean across voxels). Then we looked for 6-fold symmetric sinusoidal modulation of activity by running direction, aligned to the mean grid orientation, with the regressor $\cos(6[\theta(t)-\phi])$, on the other half of the data (see blue curve in **a**). Separate regressors were used corresponding to periods of fast, medium and slow running.



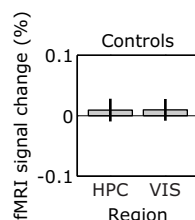
Supplementary Figure 9 | Clustering of potential grid orientations in entorhinal cortex within each participant. Polar histograms show potential grid orientations (in the range 0° and 59°, scale shown on top left plot) for all voxels in the entorhinal ROI, separately for each participant (one histogram per participant). Grid orientations were significantly clustered in 34/42 participants (Rayleigh test of uniformity, accounting for spatial smoothing, on each participant; * $P < 0.05$; (*) approaching significance at $P = 0.08$). The length of each bar indicates number of voxels with similar grid orientation; blue number indicates scale of outer circle of polar histogram.



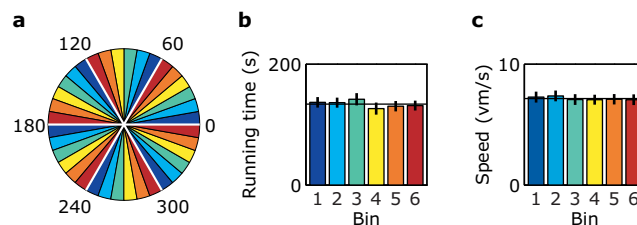
Supplementary Figure 10 | Sinusoidal modulation in left entorhinal cortex, and alignment effect and average sinusoidal modulation in left and right entorhinal cortex. **a**, Peak fMRI activation for the sinusoidal directional modulation with 6-fold rotational symmetry during fast runs in left entorhinal cortex ($-18/-12/-21$; $z = 2.96$; $P = 0.002$; image thresholded at $P < 0.01$). **b-d**, Bar plots show sinusoidal modulation for the 3 speed levels (**b**), sinusoidal modulation for the control models (fast runs, **c**), and mean signal for aligned and misaligned fast runs (**d**), all for the peak voxel in **a**. **e**, Peak fMRI activation for aligned vs misaligned fast runs in left ($-18/-12/-21$; $z = 3.14$; $P < 0.001$), top, and right entorhinal cortex ($30/3/-30$; $z = 3.47$; $P < 0.001$), bottom. Images are thresholded at $P < 0.01$; bars show mean signal for aligned and misaligned fast runs for the peak voxel in **e**. All bar plots show mean percentage fMRI signal change, see Fig. 3 in the main text for further details. **f**, Average sinusoidal modulation across all voxels is plotted separately for the whole entorhinal ROI (B, bilateral; one-tailed t -test; $P = 0.043$), the right (R; $P = 0.035$) and left (L; $P = 0.092$) hemisphere. We speculate that the right entorhinal cortex is more specialized for spatial processing, possibly like both rodent entorhinal cortices, while the left entorhinal cortex may respond more strongly to non-spatial inputs, including verbal ones. This would be consistent with the general trend of hemispheric lateralization, and with speculation regarding evolutionary adaptation of hippocampal function, see e.g. ref. 25 and Burgess et al, Neuron 2002.



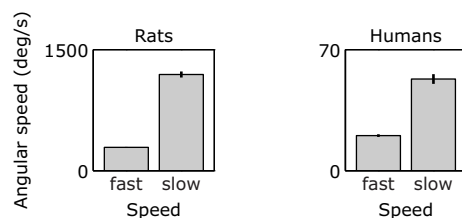
Supplementary Figure 11 | Models with different directional periodicities. Illustrations of **a**, the model with 6-fold rotational symmetry ($360^\circ/6 = 60^\circ$ periodicity) consistent with a grid cell population response, and the control models with **b**, 4-fold rotational symmetry ($360^\circ/4 = 90^\circ$ periodicity); **c**, 8-fold rotational symmetry ($360^\circ/8 = 45^\circ$ periodicity); **d**, 5-fold rotational symmetry ($360^\circ/5 = 72^\circ$ periodicity); and **e**, 7-fold rotational symmetry ($360^\circ/7 = 51.4^\circ$ periodicity), all inconsistent with grid cells. **f**, A directional modulation during fast runs in entorhinal cortex was also absent for directional periodicities of 72° and 51.4° (5-fold and 7-fold rotational symmetry) using the identical procedure as for the analysis of 60° directional modulation. Bar plots show the mean amplitude of sinusoidal modulation for the peak voxel in right (see Fig. 3a) and left (see Supplementary Fig. 10a) entorhinal cortex.



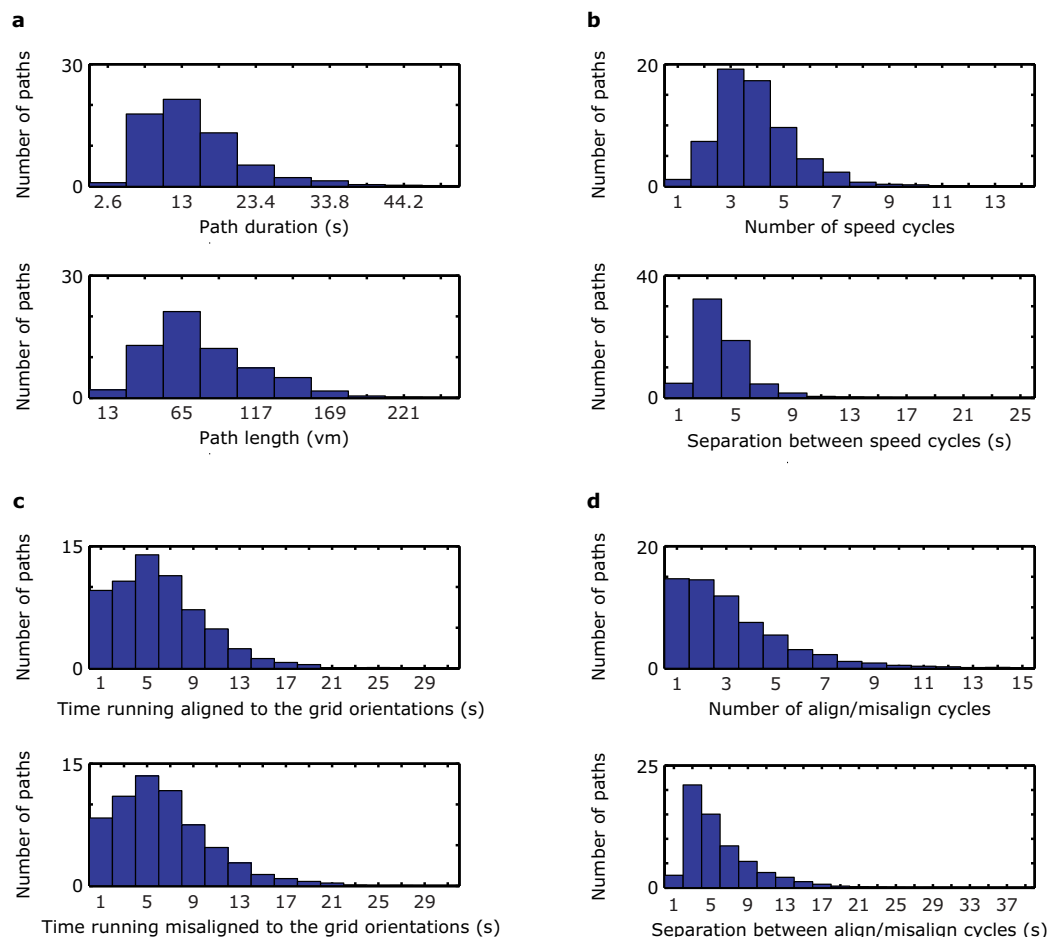
Supplementary Figure 12 | Posterior hippocampus and visual cortex activity does not show sinusoidal modulation with 6-fold rotational symmetry. We applied the same ROI analysis as was applied to entorhinal cortex (estimating mean grid orientation on one half of the data, then looking for sinusoidal modulation of activity with 6-fold rotational symmetry aligned to this orientation in the other half of the data) to two control areas. Visual cortex (which would be expected to show any effects resulting from a visual confound) and posterior hippocampus (which has been associated with spatial navigation, and might be thought to contain place cells rather than grid cells) were chosen. ROIs (8mm in radius) centred on the posterior right hippocampal location (HPC; MNI coordinates 27/-30/-3) previously associated with memory performance in this task (ref. 11) and the location of peak basic adaptation in visual cortex (VIS; see Fig. 4) were defined and subjected to the analysis. The mean response of the two control ROIs to the sinusoidal modulation regressor for fast runs is shown. There was no significant modulation, unlike for entorhinal cortex.



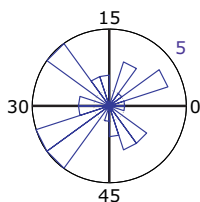
Supplementary Figure 13 | Unbiased sampling of directions. **a**, The measures of each participant's location within the VR environment were binned into 6 categories (each shown in a different colour) according to the angle of their running direction. Each bin has width 10°. **b-c**, Running time (**b**) and speed (**c**) do not differ from the average running time (all P 's > 0.6) and the average speed (all P 's > 0.8), respectively. Overall average running time and speed are indicated by a black line in **b** and **c**. vm, virtual metres.



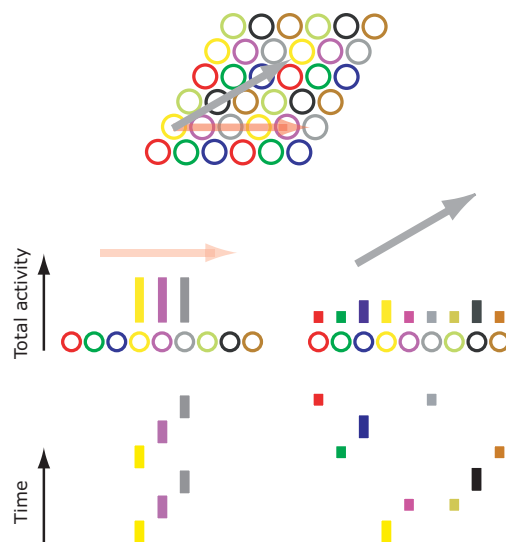
Supplementary Figure 14 | Angular speed is higher when the translational speed of animals and humans is low and vice versa. Left: Bar graph showing the rat's mean angular speed over all recording sessions that yielded grid cells. For each session half the position samples were allocated to the fast movement group and half to the slow movement group. Mean angular velocity was then calculated for each group as the instantaneous change in heading between each pair of positional points. Angular velocity at slow speeds is significantly higher than angular velocity at fast speeds (Paired t -test; $P=6.5 \times 10^{-40}$). Right: The corresponding plot for participants in the VR environment, who rotated more slowly than the rats (Paired t -test; $P < 0.001$).



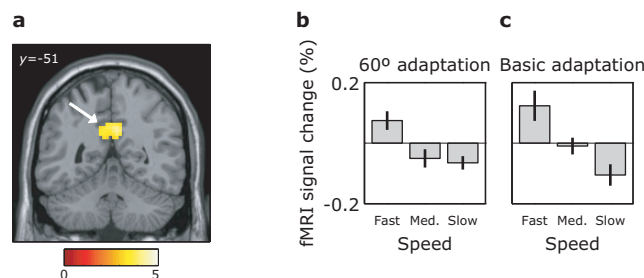
Supplementary Figure 15 | Analyses of running paths in humans. Histograms show mean **a**, path durations and path lengths (for display purposes, outliers [very long paths > 52s] were omitted from the plots), **b**, number of speed cycles (change of speed category) and temporal separation between speed cycles (1/temporal frequency of speed cycles), **c**, time running aligned and misaligned to the axes of a grid aligned to that participant's mean grid orientation and **d**, number of full align/misalign cycles and temporal separation between align/misalign cycles (1/temporal frequency of align/misalign cycles). Paths were separated by variable inter-trial intervals. vm, virtual metres.



Supplementary Figure 16 | Mean grid orientations in entorhinal cortex vary randomly between participants. Polar histogram shows that the mean grid orientations (range 0°-59°) in entorhinal cortex did not differ significantly from uniformity across participants (Rayleigh test, $P=0.35$). The length of each bar indicates number of participants with a given grid orientation; blue number indicates scale of outer circle of polar histogram.



Supplementary Figure 17 | Illustration of the effect of running direction on the dynamics of activity in a population of grid cells. For a population of evenly distributed grids the combined activity of all cells is essentially constant across all positions and directions of running. However, depending on the direction in which the animal moves the number of different grids that become active during a single run and the frequency of activity of each cell will vary. To illustrate, the centres of grid cell firing fields are shown as open circles, different colours refer to different cells. Each cell's activity (number of spikes fired) is indicated by the height of the bars shown in the corresponding colour (runs through the field centre generating twice as many spikes as runs through the edge). A run aligned with the grid (red arrow) activates fewer different cells (3 cells shown in this illustration) than a run of the same length aligned at 30° to the grid (grey arrow; 9 cells shown). Conversely, the smaller number of grids activated during aligned runs each have a higher mean activity (see bars) since they are re-activated more frequently (see bars below, indicating the timecourse of activation of cells encountered during aligned and misaligned runs).



Supplementary Figure 18 | Adaptation to runs at 60° from the current direction and basic adaptation in medial parietal cortex. **a**, 60° shifted directional adaptation in medial parietal cortex (peak: 6/-51/33; $z=4.12$). **b**, Adaptation is specific to fast runs. **c**, This region also shows adaptation to absolute running direction. In **b** and **c**, adaptation effects are shown for the peak voxel in **a** for fast, medium, and slow runs.